

# Spatiotemporal orchestration of $\text{Ca}^{2+}$ -cAMP oscillations on AKAP/AC nanodomains is governed by an incoherent feedforward loop

Lingxia Qiao<sup>1</sup>, Michael Getz<sup>2</sup>, Ben Gross<sup>1</sup>, Brian Tenner<sup>3</sup>, Jin Zhang<sup>\*4-6</sup>, and Padmini Rangamani<sup>\*1</sup>

<sup>1</sup>Department of Mechanical and Aerospace Engineering, Jacob's School of Engineering, University of California San Diego, La Jolla, CA.

<sup>2</sup>Luddy School of Informatics, Computing, and Engineering, Indiana University, Bloomington, IN.

<sup>3</sup>SomaLogic, La Jolla, CA.

<sup>4</sup>Department of Pharmacology, University of California San Diego, La Jolla, CA.

<sup>5</sup>Department of Bioengineering, University of California San Diego, La Jolla, CA.

<sup>6</sup>Department of Chemistry and Biochemistry, University of California San Diego, La Jolla, CA.

\*To whom correspondence must be addressed: [jzhang32@ucsd.edu](mailto:jzhang32@ucsd.edu) and [prangamani@ucsd.edu](mailto:prangamani@ucsd.edu)

## Abstract

The nanoscale organization of enzymes associated with the dynamics of second messengers is critical for ensuring compartmentation and localization of signaling molecules in cells. Specifically, the spatiotemporal orchestration of cAMP and  $\text{Ca}^{2+}$  oscillations is critical for many cellular functions. Previous experimental studies have shown that the formation of nanodomains of A-kinase anchoring protein 79/150 (AKAP150) and adenylyl cyclase 8 (AC8) on the surface of pancreatic MIN6  $\beta$  cells modulates the phase of  $\text{Ca}^{2+}$ -cAMP oscillations. In this work, we develop computational models of

the  $\text{Ca}^{2+}$ /cAMP pathway and AKAP/AC nanodomain formation that give rise to two important predictions: first, the in-phase and out-of-phase oscillations associated with  $\text{Ca}^{2+}$ -cAMP dynamics on and away from the nanodomains can be explained by an incoherent feedforward loop. Second, the formation of these nanodomains can be explained by Turing patterns. Factors such as cellular surface-to-volume ratio, compartment size, and distance between nanodomains do not affect the existence of in-phase or perfectly out-of-phase  $\text{Ca}^{2+}$ /cAMP oscillation, but some of these factors can affect the time delay for the perfectly out-of-phase  $\text{Ca}^{2+}$ /cAMP oscillation. Finally, we predict that both the Turing pattern-generated nanodomains and experimentally measured nanodomains demonstrate the existence of in-phase and perfectly out-of-phase  $\text{Ca}^{2+}$ /cAMP oscillation when the AC8 is at a low level, consistent with the behavior of an incoherent feedforward loop. These findings unveil the key circuit motif that governs cAMP and  $\text{Ca}^{2+}$  oscillations and advance our understanding of how nanodomains can lead to spatial compartmentation of second messengers.

## 1 Introduction

Cyclic adenosine monophosphate (cAMP) and  $\text{Ca}^{2+}$  are key second messengers that regulate several cellular functions, including muscle contraction, neuronal excitability, cell migration, metabolism, endocytosis, plasma membrane repair, and immune function [1, 2, 3, 4, 5, 6]. The execution of these cellular functions relies on both the temporal dynamics and the spatial distribution of cAMP and  $\text{Ca}^{2+}$ . The temporal dynamics of cAMP and  $\text{Ca}^{2+}$  play crucial roles in many biological systems. For example, changes in the cAMP level and downstream protein kinase A (PKA) are connected with tumorigenesis, invasion, metastasis and drug resistance [7, 8, 9], and an increase in cAMP levels inhibits hepatocellular carcinoma cell proliferation [10] and induces the apoptosis of glioblastoma cells [11];  $\text{Ca}^{2+}$  frequency can be decoded by downstream  $\text{Ca}^{2+}$  sensors and translated into distinct cellular responses [12, 13, 14, 15, 16]. In addition to tightly regulated temporal control, cAMP and  $\text{Ca}^{2+}$  are highly spatially compartmentalized at the plasma membrane and cellular organelles [17, 18, 19]. If this spatial compartmentalization is disrupted, it may lead to changes in signaling pathways and gene expression [20, 21, 22], as well as pathological conditions such as cell apoptosis [22], abnormal insulin secretion [23], heart dysfunction [3, 24, 25], familial breast cancer [26], and schizophrenia [27].

The temporal dynamics of cAMP and  $\text{Ca}^{2+}$  usually demonstrate oscillatory behaviors in many

cell types including neurons [28, 29], cardiomyocytes [30], and pancreatic  $\beta$  cells [31]. Given the importance of spatiotemporal orchestration of  $\text{Ca}^{2+}$  and cAMP function, understanding the biochemical and biophysical mechanisms that govern their oscillations is very important. Mathematical and computational modeling can aid in deciphering how different cellular features play a role in governing these oscillations [32, 33, 34, 35, 36, 37]. Previously, we showed that the frequency of  $\text{Ca}^{2+}$ -cAMP oscillations depends on the geometry of dendritic spines in neurons [38, 39]. In this study, we focus on cAMP and  $\text{Ca}^{2+}$  oscillations in pancreatic  $\beta$  cells because of their critical role in insulin secretion. The pathway regulating the insulin secretion in pancreatic  $\beta$  cells is as follows: an increase in blood glucose leads to the increase in the cytosolic ATP/ADP ratio in the pancreatic  $\beta$  cell [40]; then, ATP-sensitive potassium channel ( $\text{K}_{\text{ATP}}$ ) channel closes, inducing the influx of  $\text{Ca}^{2+}$  and subsequent insulin vesicle exocytosis [41, 42]. During this insulin secretion process, the cAMP pathway is also activated: increased  $\text{Ca}^{2+}$  level also stimulates the activation of adenylyl cyclase type 8 (AC8), and AC8 improves the cAMP production, followed by protein kinase A (PKA) activation. Furthermore, cAMP level is also controlled by the  $\text{Ca}^{2+}$ -dependent PDE1C (phosphodiesterase 1C; denoted as PDE for simplicity) in pancreatic  $\beta$  cells, because this PDE is activated by  $\text{Ca}^{2+}$  and then mediates the transient cAMP decreases [32]. The activated cAMP/PKA pathway affects cellular excitability,  $\text{Ca}^{2+}$  signals, exocytosis, cell viability, and cell–cell interactions [31, 43, 44]. Disturbances in this pathway may be associated with diabetes [45].

The cross-talk between  $\text{Ca}^{2+}$  and cAMP is vital for the proper function of pancreatic  $\beta$  cells. Such cross-talk is achieved by the highly connected spatiotemporal organization between cAMP and  $\text{Ca}^{2+}$  in pancreatic  $\beta$  cells. On the one hand, the temporal dynamics of  $\text{Ca}^{2+}$  and cAMP in pancreatic  $\beta$  cells show synchronized oscillations, and this oscillation is initiated and modulated by PKA [46]. Recently, experiments showed that the synchronized oscillation of these two second messengers exhibits distinct phase delay at different membrane locations. For example, the membrane nanodomain formed by plasma membrane (PM)-localized scaffold protein A-kinase anchoring protein 79 (AKAP79; rodent ortholog AKAP150) [32] (Figure 1A). AKAP79/150 is a multivalent scaffold protein that associates with itself to form nanodomains. Additionally, AKAP79/150s also can recruit signaling molecules to cell membrane, including PKA, the voltage-gated  $\text{Ca}^{2+}$  channel  $\text{Ca}_v1.2$ , Protein Kinase C (PKC), the  $\text{Ca}^{2+}$ /calmodulin-dependent protein phosphatase calcineurin,  $\text{Ca}^{2+}$ -sensitive ACs, and AMPA receptors [47]. On membrane nanodomains formed by A-kinase anchoring proteins 79/150 (AKAP79/150) and AC8 (referred to as the AKAP/AC nanodomains),  $\text{Ca}^{2+}$  and cAMP were found to oscillate in-

phase, i.e., without any phase difference. Away from the membrane AKAP/AC nanodomains,  $\text{Ca}^{2+}$  and cAMP oscillate out-of-phase. This discovery that membrane nanodomains of AKAP79/150 and AC8 can modulate the in- and out-of-phase oscillations of cAMP- $\text{Ca}^{2+}$  leads to interesting questions about the biochemical and biophysical mechanisms that regulate the formation of these nanodomains and coordinate the spatiotemporal dynamics of these critical second messengers. Can the dynamics of in- and out-of-phase oscillations of  $\text{Ca}^{2+}$  and cAMP be explained by a simple network motif? Does subcellular compartment size affect these phase shifts? How do patterns of nanodomains form on the membrane and how do multiple nanodomains affect these oscillatory patterns? We sought to answer these questions using computational modeling.

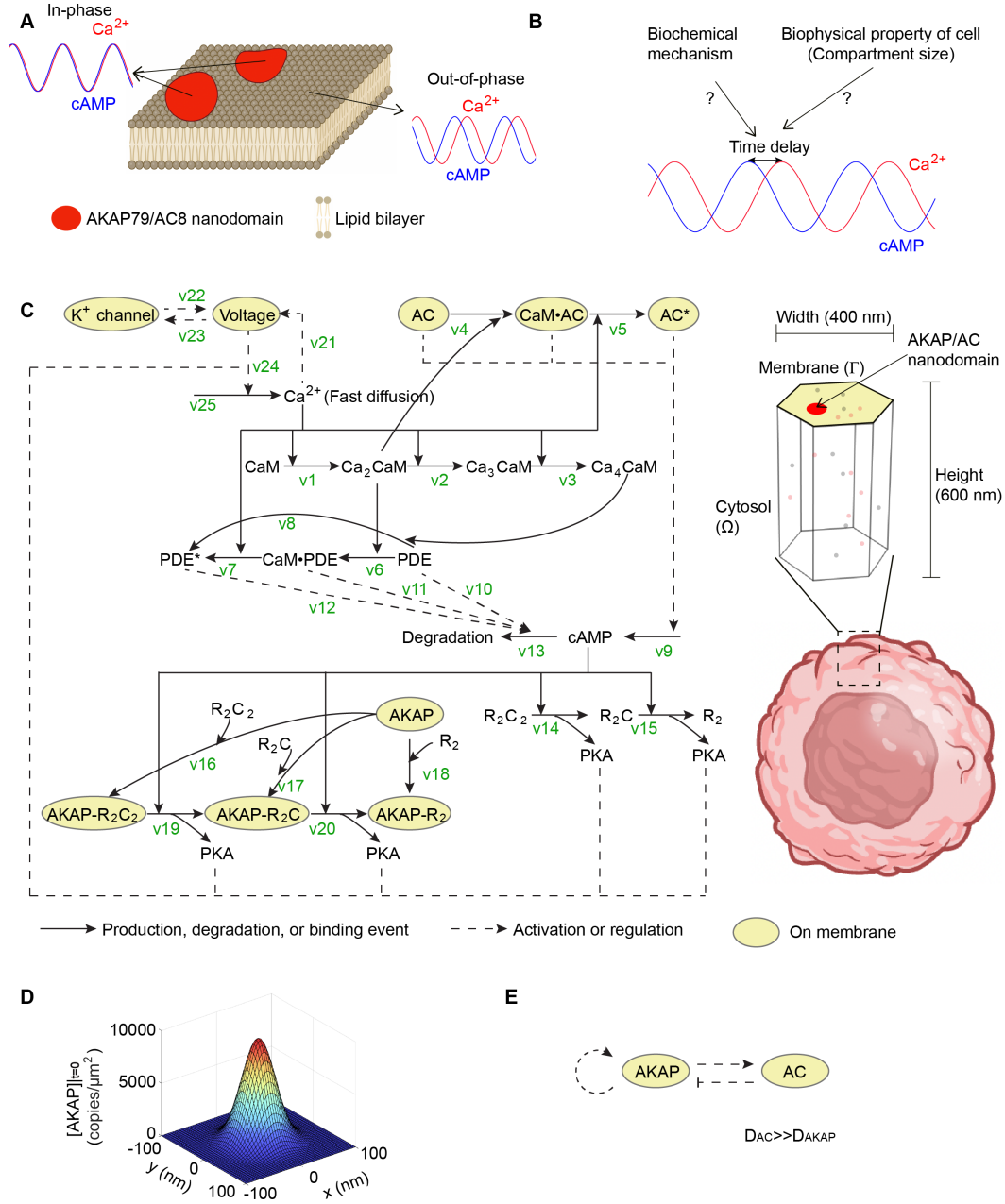


**Figure 1: The phase regulation of  $\text{Ca}^{2+}$ -cAMP oscillation and corresponding mathematical modeling.** (A) Schematic showing out-of-phase  $\text{Ca}^{2+}$ -cAMP oscillation outside the nanodomain and in-phase behavior when localized to AKAP/AC nanodomains. This schematic is designed based on experiments in [32] (created with BioRender.com). (B) In this work, we aim to explore the biochemical mechanism of the phase difference (or time delay) between  $\text{Ca}^{2+}$  and cAMP oscillation and study the possible contributing factors. (C) Mathematical modeling of the AKAP- $\text{Ca}^{2+}$ -cAMP circuit. On the left-hand side, the diagram of the signaling pathway is shown; the solid arrow indicates production, degradation, or binding events, and the dashed arrow indicates the regulation effect that usually does not consume the reactants. On the right-hand side, the simulation domain is a hexagonal prism, which is only a small compartment of one cell (created with BioRender.com). In this compartment, the top surface (yellow area) denotes the cell membrane; the AKAP/AC nanodomain (the large patch in red) is located on the cell membrane; the volume under the top surface is cytosol. Molecules (dots in gray and orange) can diffuse in the cytosol or on the membrane depending on the location of the molecule. (D) A single AKAP/AC nanodomain was modeled using a Gaussian distribution. (E) Interactions between AC and AKAP that can generate a Turing pattern.

## 2 Results

In this work, we developed two classes of models – a 3D reaction-diffusion model to simulate the dynamics of cAMP and  $\text{Ca}^{2+}$  and a Turing pattern model with steric hindrance to simulate the formation of AKAP/AC nanodomains. For the 3D reaction-diffusion model, we defined preexisting AKAP/AC nanodomains and focused on the dynamics of cAMP and  $\text{Ca}^{2+}$ . We used this model to investigate how activities of AC and PDE, cellular compartment size, and pattern of nanodomains affect the in- and out-of-phase oscillations of  $\text{Ca}^{2+}$  and cAMP (Figure 1B). To understand how nanodomains might form, we used a Turing model with steric repulsion [48] to characterize the regimes in which stable AKAP/AC nanodomains might arise. Finally, to investigate how the nanodomain patterns might affect the in- and out-of-phase oscillations, we used patterns from both the Turing model and experimentally generated STORM data as the initial distribution of AKAP/AC nanodomains and predicted that both the pattern of AKAP/AC nanodomains and AC activities are critical in controlling the phase behavior of  $\text{Ca}^{2+}$ -cAMP. These results provide insights into the biochemical and biophysical mechanisms that

regulate the spatiotemporal dynamics of  $\text{Ca}^{2+}$  and cAMP.

## 2.1 Phase oscillations of $\text{Ca}^{2+}$ and cAMP are driven by active AC and PDE

We first simulated the dynamics of  $\text{Ca}^{2+}$  and cAMP using the 3D reaction-diffusion model described in Section S1. We briefly describe the model below. We considered 22 state variables in total (Figure 1C), where 13 chemical species are in the cytosol (non-highlighted species in Figure 1C) and the rest are on the membrane (highlighted in yellow in Figure 1C). The reactions among these chemical species are briefly introduced below (See Section S1 for details): the increase of  $\text{Ca}^{2+}$  in the cytosol leads to the activation of inactive PDE (Cyclic nucleotide phosphodiesterase) in the cytosol (v4-5) and inactive AC (Adenylyl cyclase) on AKAP/AC nanodomains through CaM (calmodulin) (v1-3 and v6-8); next, the active AC (denoted as  $\text{AC}^*$ ) on AKAP/AC nanodomains enhances the synthesis of cAMP (v9), and the active PDE (denoted as  $\text{PDE}^*$ ) improves the degradation of the cAMP in the cytosol (v10-13); the change in the cAMP level will affect PKA (protein kinase A) in the cytosol (v14-20), and the latter will regulate the dynamics of  $\text{Ca}^{2+}$  by interacting with membrane voltage (v21-25). These reactions include negative feedback, incoherent feedback loop, and Hodgkin-Huxley model, and thus are able to generate oscillation. The settings for AKAP/AC nanodomain and compartment are the same as the calculations in [32]: at time 0 there is only one AKAP/AC nanodomain located at the center of the cell membrane, which is modeled by a Gaussian distribution with standard deviation of 25 nm (Section S1 and Figure 1D); the compartment has a height of 600 nm and width of 400 nm (Section S1 and Figure 2A). Furthermore, we chose periodic boundaries for the six surfaces surrounding the compartment, so that many compartments can assemble to form a large cell domain without any discontinuity.

Next, we used the above model to simulate the dynamics of  $\text{Ca}^{2+}$  and cAMP when there is only one AKAP/AC nanodomain existing in the center of the membrane. Since the cAMP dynamics at the cell membrane have been experimentally well studied in [32], we also focused on the dynamics of  $\text{Ca}^{2+}$  and cAMP at the cell membrane. Due to the radial symmetry of the AKAP/AC nanodomain, we only need to focus on dynamics in the line from the center to the right edge of the cell membrane (white line in Figure 2B) and used  $x$  to denote the distance from the center to the location of interest at cell membrane. We found that, the time delay between  $\text{Ca}^{2+}$  and cAMP peak time is zero when  $x = 0$  and near 25 seconds when  $x$  is larger than 50 nm (Figure 2B), indicating the in-phase behavior at the AKAP/AC nanodomain and out-of-phase behavior outside AKAP/AC nanodomain. This conclusion is

consistent with the simulation results in [32]. The transition happens at  $x=48$  nm, which is nearly two times of standard deviation of the Gaussian distribution; this suggests that the out-of-phase behavior also occurs at a low but non-zero level of AC\*.

To explore why there is a sharp transition of the time delay when changing from AKAP/AC nanodomain to the general membrane, we plotted the normalized dynamics of  $\text{Ca}^{2+}$  and cAMP when  $x = 0, 49,$  and  $200$  nm (Figure 2C). Here, normalization indicates that the concentration is divided by the maximum value at a specific location during the time interval  $[0, 1200]$  seconds. The dynamics of  $\text{Ca}^{2+}$  remain unchanged at different locations (red lines in Figure 2C) because of the fast diffusion of  $\text{Ca}^{2+}$ . In contrast, the dynamics of cAMP are different at different locations: peaks of cAMP at  $x = 0$  are in-phase with  $\text{Ca}^{2+}$ , those at  $x = 49$  nm are either in-phase or out-of-phase with  $\text{Ca}^{2+}$  and those at  $x = 200$  nm are out-of-phase with  $\text{Ca}^{2+}$ . Here, out-of-phase behavior denotes any non-zero difference in the phase between two oscillatory trajectories. These results indicate that the in-phase peak dominates on the AKAP/AC nanodomain while the out-of-phase peak dominates outside the AKAP/AC nanodomain.



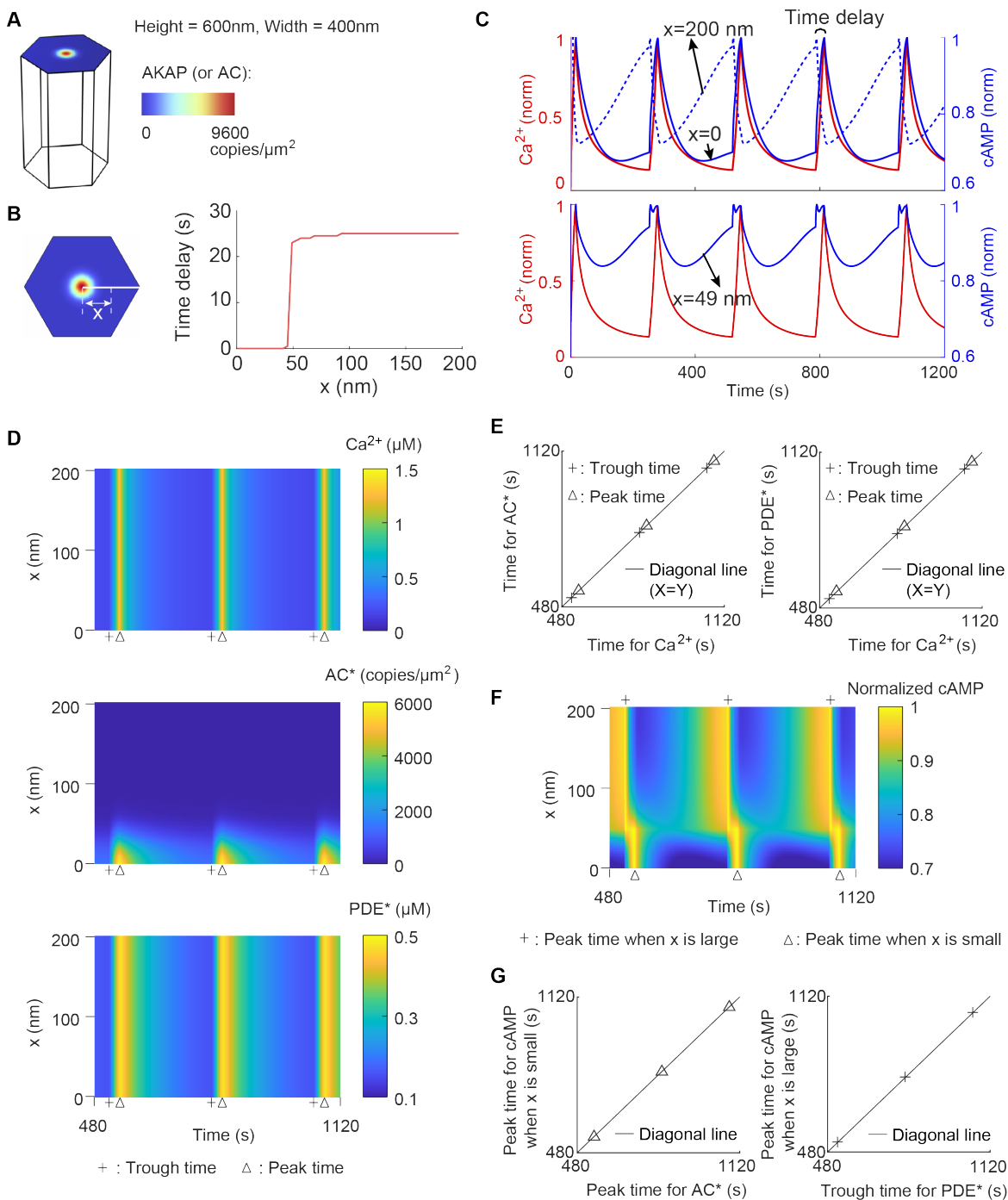


**Figure 2: Phase oscillations of  $\text{Ca}^{2+}$  and cAMP are driven by active AC and PDE.** (A) The simulation domain and initial condition of AC and AKAP. The compartment and the assumption of one AKAP/AC nanodomain are the same as those in [32]. (B) The time delay between  $\text{Ca}^{2+}$  and cAMP as a function of the distance  $x$  to the AKAP/AC nanodomain. The time delay is defined as the difference of peak time between  $\text{Ca}^{2+}$  and cAMP. (C) The dynamics of  $\text{Ca}^{2+}$  (in red) and cAMP (in blue) at  $x = 0$ ,  $x = 49$  nm, and  $x = 200$  nm. For better visualization, the dynamics at  $x = 49$  are plotted in a separate panel (lower panel). (D) Kymographs depicting the dynamics for  $\text{Ca}^{2+}$ , active AC (AC\*), and active PDE (PDE\*) at different locations at the cell membrane. The x coordinate is the time, and the y coordinate is the distance  $x$  present in (B). Trough time and peak are indicated by a plus sign and triangle, respectively. Here, the peak time is the time when the concentration of species reaches the maximal value, and the trough time the minimal value. (E) Comparisons between  $\text{Ca}^{2+}$  trough time and AC\* trough time (left; plus sign), between  $\text{Ca}^{2+}$  peak time and AC\* peak time (left; triangle), between  $\text{Ca}^{2+}$  trough time and PDE\* trough time (right; plus sign), and between  $\text{Ca}^{2+}$  peak time and PDE\* peak time (right; triangle). The diagonal line indicates the equality of the x-axis and y-axis. (F) Kymograph depicting cAMP dynamics. The color intensity indicates the normalized cAMP level. The plus sign and triangle denote the cAMP peak time when  $x$  is large and small, respectively. (G) Comparisons between AC\* peak time and cAMP peak time on the AKAP/AC nanodomain (left), and between PDE\* trough time and cAMP peak time outside the AKAP/AC nanodomain (right).

To understand the kinetics of in-phase and out-of-phase cAMP peaks, we first analyzed the dynamics of the immediate upstream species:  $\text{Ca}^{2+}$ , active AC (AC\*), and active PDE (PDE\*). We plotted the dynamics of concentrations of these three species at the cell membrane (Figure 2D), and then calculated the trough and peak time (marked by the plus sign or triangle). Here, the trough (or peak) time is defined as the time when the concentration of species reaches the minimum (or maximum) value. For  $\text{Ca}^{2+}$ , due to its fast diffusion, the trough and peak times remain unchanged when the location  $x$  varies (upper panel in Figure 2D). As for AC\*, its peak and trough times also do not change when the location  $x$  varies between 0 and 20 nm, but these peak and trough times cannot be defined at  $x > 20$  nm because of the low AC\* level outside the AKAP/AC nanodomain (middle panel in Figure 2D). The PDE\* shows similar behavior as  $\text{Ca}^{2+}$ , that is, the trough and peak times for PDE\* are fixed no matter how the location  $x$  changes (lower panel in Figure 2D). Next, we compared these times

between  $\text{Ca}^{2+}$  and  $\text{AC}^*$  and between  $\text{Ca}^{2+}$  and  $\text{PDE}^*$  (Figure 2E). We found that, the  $\text{AC}^*$  trough time at  $x < 20$  nm is the same as that for  $\text{Ca}^{2+}$ , and so is the peak time (left panel in Figure 2D). Similarly, the trough and peak times for  $\text{PDE}^*$  also match the trough and peak times for  $\text{Ca}^{2+}$ , respectively (right panel in Figure 2D). These consistencies in the trough and peak time may be caused by the strong activation from  $\text{Ca}^{2+}$  to  $\text{AC}^*$  (v4-5 in Table S2) and from  $\text{Ca}^{2+}$  to  $\text{PDE}^*$  (v1-8 in Table S2). Furthermore, these consistencies indicate that the  $\text{AC}^*$  on the nanodomain and  $\text{PDE}^*$  at the entire membrane exhibit in-phase oscillation with  $\text{Ca}^{2+}$ .

After analyzing the dynamics of upstream species of cAMP, we turned to explore how these dynamics may affect in-phase and out-of-phase behaviors of cAMP. We plotted the dynamics of the normalized cAMP level at different locations at the cell membrane (Figure 2F), and then compared the cAMP peak time with  $\text{PDE}^*$  trough time or  $\text{AC}^*$  peak time (Figure 2G). The cAMP concentration for each  $x$  is normalized by the maximal value during the entire time interval [0, 1200] seconds. From the dynamics of the normalized cAMP level (Figure 2F), we can find that the cAMP peak time shifts from left to right when the location  $x$  decreases. Moreover, the cAMP peak time is the same as the  $\text{AC}^*$  peak time when  $x$  is small (left panel in Figure 2G), but equal to the  $\text{PDE}^*$  trough time when  $x$  is large (right panel in Figure 2G). These results suggest the in-phase  $\text{AC}^*$ -cAMP oscillation on the AKAP/AC nanodomain and perfectly out-of-phase  $\text{PDE}^*$ -cAMP oscillation outside the AKAP/AC nanodomain. Since  $\text{AC}^*$  catalyzes the cAMP synthesis (v9 in Table S2) and  $\text{PDE}^*$  enhances the cAMP degradation (v12 in Table S2), these perfectly out-of-phase and in-phase behaviors may result from the competition between  $\text{AC}^*$ -induced cAMP production and  $\text{PDE}^*$ -induced cAMP degradation. On the AKAP/AC nanodomain, the  $\text{AC}^*$  level is much higher than  $\text{PDE}^*$ , and thus the activation from  $\text{AC}^*$  dominates, leading to in-phase  $\text{AC}^*$ -cAMP oscillation. In contrast, outside the AKAP/AC nanodomain, the  $\text{AC}^*$  shows low values, and thus the cAMP levels are mainly governed by the action of  $\text{PDE}^*$ ;  $\text{PDE}^*$  inhibits the cAMP level by enhancing the cAMP degradation, resulting in perfectly out-of-phase  $\text{PDE}^*$ -cAMP oscillation. When combined with the observation of in-phase  $\text{Ca}^{2+}$ - $\text{AC}^*$  oscillation on the nanodomain and in-phase  $\text{Ca}^{2+}$ - $\text{PDE}^*$  oscillation at the entire membrane, the cAMP is in-phase with  $\text{Ca}^{2+}$  on the AKAP/AC nanodomain but perfectly out-of-phase with  $\text{Ca}^{2+}$  outside the AKAP/AC nanodomain.

## 2.2 Experimental data supports model predictions of in- and perfectly out-of-phase $\text{Ca}^{2+}$ -cAMP oscillations

We summarized the mechanism of in-phase and perfectly out-of-phase  $\text{Ca}^{2+}$ -cAMP oscillations in Figure 3A. The origin of the stimulus is the  $\text{Ca}^{2+}$  oscillation, which is uniformly distributed spatially due to rapid diffusion.  $\text{Ca}^{2+}$  dynamics affects the phase of the cAMP by two species AC\* and PDE\*, whose dynamics are as follows: the PDE\* oscillation at the entire cell membrane is in-phase with  $\text{Ca}^{2+}$  through the activation from  $\text{Ca}^{2+}$  to PDE\* (v1-3 and v6-8 in Table S2). On the AKAP/AC nanodomain, AC\* is not only in high concentration but also in-phase with  $\text{Ca}^{2+}$  since the  $\text{Ca}^{2+}$  catalyzes the activation of AC\* (v4-5 in Table S2) whereas outside the AKAP/AC nanodomain, AC\* is in low concentration, because AC is in low concentration outside the AKAP/AC nanodomain. As a result, on the AKAP/AC nanodomain, the enriched AC\* enhances the cAMP production (v9 in Table S2), driving the cAMP oscillation become in-phase with AC\*; outside the nanodomain, the AC\* level is much smaller than the PDE\* level, and the latter degrades cAMP (v12 in Table S2), causing perfectly out-of-phase cAMP oscillation with PDE\*. Since AC\* on the nanodomain and PDE\* on the entire membrane are both in-phase with  $\text{Ca}^{2+}$ , the cAMP oscillation is also in-phase with  $\text{Ca}^{2+}$  on the nanodomain and perfectly out-of-phase with  $\text{Ca}^{2+}$  outside the nanodomain.

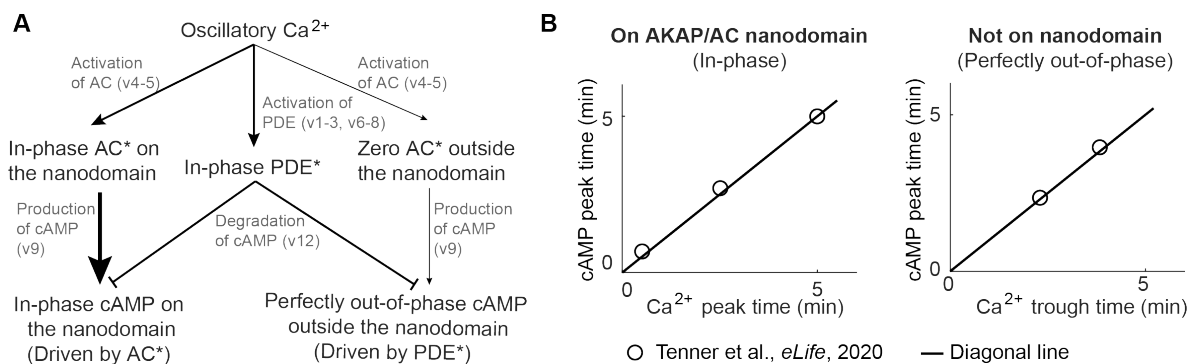


**Figure 3: Experimental data supports model predictions of in- and perfectly out-of-phase  $\text{Ca}^{2+}$ -cAMP oscillations.** (A) Schematic of the dependence of time delay between  $\text{Ca}^{2+}$  and cAMP on the interplay between active AC and PDE. The arrow thickness indicates the regulation strength: the thicker the arrow is, the stronger the regulation is. On the AKAP/AC nanodomain, the active AC dominates, driving the in-phase  $\text{Ca}^{2+}$ -cAMP oscillation. However, the active PDE dominates outside the AKAP/AC nanodomain, leading to perfectly out-of-phase  $\text{Ca}^{2+}$ -cAMP oscillation. (B) The experimentally observed in-phase  $\text{Ca}^{2+}$ -cAMP oscillation on the AKAP/AC nanodomain and perfectly out-of-phase  $\text{Ca}^{2+}$ -cAMP oscillation outside the AKAP/AC nanodomain. The in-phase  $\text{Ca}^{2+}$ -cAMP oscillation is illustrated by the same cAMP peak time and  $\text{Ca}^{2+}$  peak time; the perfectly out-of-phase  $\text{Ca}^{2+}$ -cAMP oscillation is indicated by the same cAMP peak time and  $\text{Ca}^{2+}$  trough time. These peak or trough time data (circular markers) are from Tenner et al., *eLife*, 2020[32], and the black line denotes the diagonal line.

We tested the model predictions against previously published experimental data in [32]. First, we extracted the time when the response of the cAMP biosensor reaches the highest value, and then denoted this time as the cAMP peak time. In [32], two types of cAMP biosensors were used. The AKAP/AC nanodomain-specific cAMP biosensor provides the cAMP peak time on the AKAP/AC nanodomain, and the plasma membrane-specific cAMP biosensor gives the cAMP peak time outside the AKAP/AC nanodomain. These peak times from two types of cAMP biosensors are the y-coordinates in Figure 3B. Next, we extracted the time when the response of the  $\text{Ca}^{2+}$  biosensor reaches the highest value and lowest value, and denoted them as  $\text{Ca}^{2+}$  peak and  $\text{Ca}^{2+}$  trough time respectively (x coordinates in Figure 3B). We found that the cAMP peak time on the AKAP/AC nanodomain is close to  $\text{Ca}^{2+}$  peak time (left panel in Figure 3B), suggesting the in-phase  $\text{Ca}^{2+}$ -cAMP oscillation. However, the cAMP peak time outside the AKAP/AC nanodomain is the same as the  $\text{Ca}^{2+}$  trough time (right panel in Figure 3B). This means that the phase difference between the  $\text{Ca}^{2+}$  and cAMP is exactly half of the period, which is perfectly out-of-phase. Therefore, these experiment results are consistent with the numerical predictions from our model with respect to the in-phase and perfectly out-of-phase  $\text{Ca}^{2+}$ -cAMP oscillation. It should be noted that, although the in-phase behavior has been extensively studied in [32], the perfect property of the out-of-phase behavior was first discovered in this work.

### 2.3 A simple incoherent feedforward loop explains in-phase oscillation and perfectly out-of-phase oscillation

The above analyses demonstrate the role of AC\* and PDE\* in regulating the phase difference between Ca<sup>2+</sup> and cAMP. However, the complexity of the biochemical circuit involved in the regulation of Ca<sup>2+</sup> and cAMP dynamics (Figure 1C) prevents us from identifying if AC\* and PDE\* are sufficient conditions for such phase regulation. We next investigated if a simple circuit model could shed light on the main control elements of the phase difference. The signal, which mimics Ca<sup>2+</sup> concentration, is set to be a sine wave plus a constant 1.1, where the constant 1.1 ensures the positive sign of the signal (Figure 4A). Furthermore, we assumed that the signal affects output paradoxically. On one hand, the signal improves the production of output and on the other hand, the signal increases the output degradation (Figure 4B). The circuit with two pathways with opposite effects from the input to the output is usually called as incoherent feedforward loop [49], and can exhibit different biological functions under certain conditions [49, 50, 51, 52, 53, 54, 55, 56]. These regulatory reactions are used to mimic the effect of Ca<sup>2+</sup> on cAMP caused by AC\* and PDE\*: Ca<sup>2+</sup> enhances the cAMP production by the activation of AC; at the same time, Ca<sup>2+</sup> improves the cAMP degradation by the activation of PDE. Therefore, the output can be regarded as the cAMP. The mathematical model of this simple incoherent feedforward loop is written as follows:

$$\frac{dx}{dt} = vS(t) + k_1 - m[S(t) + k_2]x \quad (1)$$

where  $S(t)$  and  $x$  denote the concentration of signal and output, respectively.  $v$  is the activation strength caused by signal,  $k_1$  is the basal production rate constant,  $m$  is the degradation rate constant and  $k_2$  captures the feedback of  $x$  on the degradation. Without loss of generality, we can set  $m = 1$  and obtain (see Section S2 for details):

$$\frac{dx}{dt} = vS(t) + k_1 - [S(t) + k_2]x. \quad (2)$$

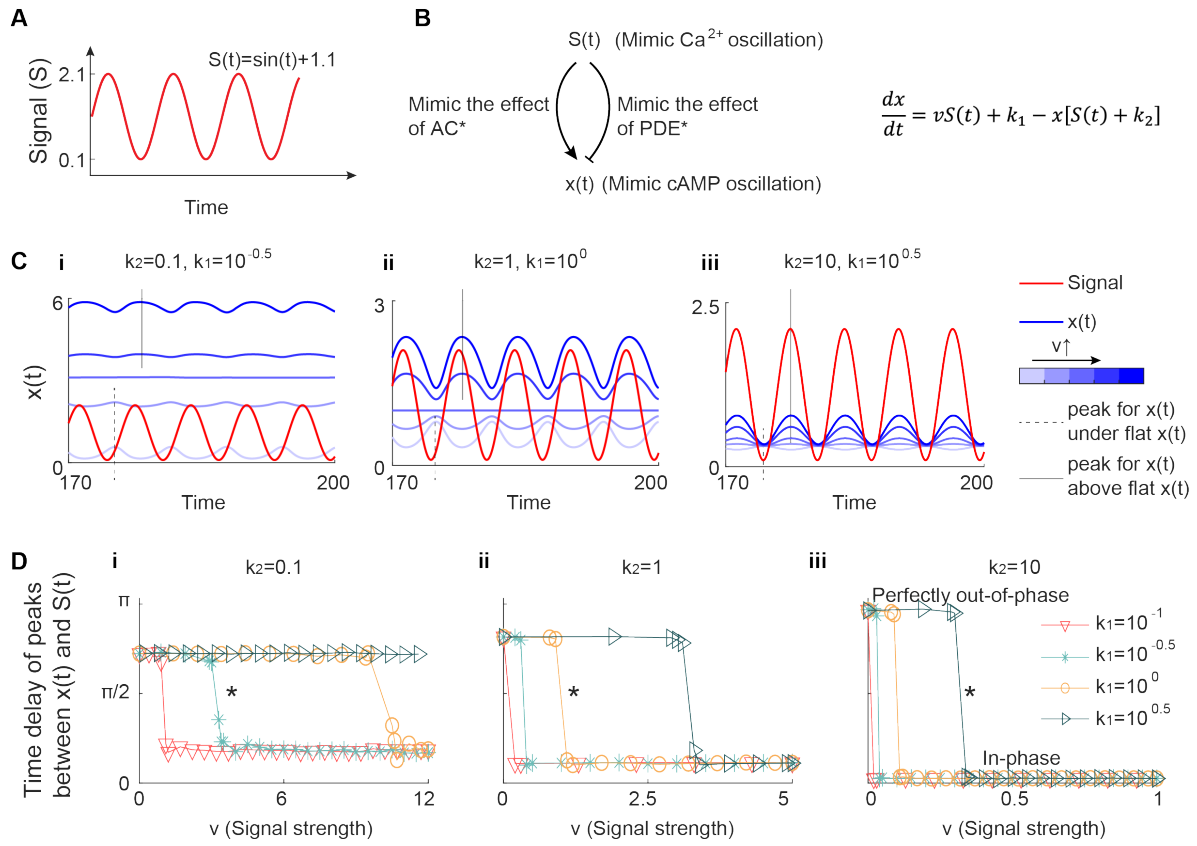


**Figure 4: A simple incoherent feedforward loop explains in-phase oscillation and perfectly out-of-phase oscillation.** (A) The signal used in the simple ODE model. We used a sine wave  $\sin(t) + 1.1$  as the signal  $S(t)$  to mimic the dynamics of  $\text{Ca}^{2+}$ , where 1.1 is to ensure the positive sign of the signal. (B) Schematic of the ODE model. We constructed a simple circuit with only two regulatory links: one is the activation from the signal  $S(t)$  to the output  $x(t)$ ; the other is the inhibition from the signal  $S(t)$  to the output  $x(t)$ . This circuit captures the positive role of  $\text{Ca}^{2+}$  not only in the cAMP production through active AC but also in the cAMP degradation through active PDE. The equation describing the dynamics of  $x(t)$  is shown in the right panel. (C) The dynamics of  $S(t)$  (red) and  $x(t)$  (blue) under different values of  $k_1$  and  $k_2$ , and  $v$ . Values of  $k_1$  and  $k_2$  are labeled over the plots. Values of  $v$  are indicated by the intensity of blue color (the darker the blue is, the higher the  $v$  is):  $v = [0, 2, 3.1, 4, 6]$  (i),  $v = [0, 0.5, 1, 2, 3]$  (ii), and  $v = [0, 0.5, 1, 2, 3]$  (iii). The trough and peak of  $x(t)$  are marked by the dashed and solid lines, respectively. (D) The time delay between  $S(t)$  and  $x(t)$  as a function of the signal strength  $v$  for different values of  $k_1$  and  $k_2$ . Three values of  $k_2$  are considered: 0.1 (i), 1 (ii), and 10 (iii). In each panel,  $k_1$  is changed from  $10^{-1}$  to  $10^{0.5}$ , shown in different colors and markers. The stars in each panel indicate the parameters used in (C).

This first-order linear ODE lacks a closed form solution. Therefore, we turned to numerical solutions to evaluate how the different parameters affected the output as a function of the input. We varied the value of the activation strength  $v$ , which mimics the effect of  $\text{AC}^*$ , from small (away from the nanodomain) to large (center of the nanodomain). We postulated that if the oscillation behavior of  $x(t)$  is perfectly out-of-phase with small  $v$  and then becomes in-phase with increased  $v$ , then this simple incoherent feedforward loop is sufficient to generate similar results observed in the 3D reaction-diffusion model. We found that, with small values of the basal production rate constant  $k_1$  and the  $x$ -induced degradation rate  $k_2$ , increasing activation strength  $v$  cannot lead to the transition from perfectly out-of-phase to in-phase behavior between the input and output (Figure 4C (i-ii)), but given large  $k_1$  and  $k_2$  we can recover the proposed  $v$  dependence (Figure 4C (iii)). In Figure 4C (iii), when  $v$  is small, the output peak time is the same as the signal trough time (the dashed line in Figure 4C (iii)), indicating the perfectly out-of-phase oscillation; when  $v$  is large, the output peak time is the signal peak time (the solid line in Figure 4C (iii)), suggesting an in-phase oscillation. However, we didn't observe the emergence of two peaks given the kinetic parameters, which were found during the



transition from in-phase to perfectly out-of-phase oscillation (lower panel in Figure 2C). The failure to observe two peaks in the simple ODE model may be because this simple ODE model neglects other reactions that also consume cAMP, such as the binding of cAMP and  $R_2C_2$  (v14 in Figure 1C), the binding of cAMP and AKAP- $R_2C_2$  (v19 in Figure 1C). To quantitatively identify the phase difference, we calculated the time delay of peaks between  $x(t)$  and  $S(t)$  for several combinations of  $k_1$  and  $k_2$  (Figure 4D). The relationship between the time delay and phase behavior is as follows – if the time delay is half of the signal period, that is,  $\pi$ , the perfectly out-of-phase oscillation is achieved while zero time delay corresponds to the in-phase oscillation. We found that the  $x$ -induced degradation rate  $k_2$  is more important than the basal production rate constant  $k_1$  in producing the desired  $v$  dependence. If  $k_2$  is small, it is impossible to achieve perfectly out-of-phase and in-phase oscillations even with different values of  $k_1$  (Figure 4D (i-ii)); only the large  $k_2$  can lead to perfectly out-of-phase and in-phase oscillations under different values of  $v$  (Figure 4D (iii)). Furthermore, the role of the basal production rate constant  $k_1$  is to shift the critical value of activation strength  $v$  that causes the transition from the perfectly out-of-phase to the in-phase. In conclusion, the exploration of the simple incoherent feedforward loop not only validates the sufficiency of the role of AC\* and PDE\* in driving phase difference, but also suggests the mechanism of perfectly out-of-phase and in-phase oscillations — a large basal degradation rate (i.e.,  $k_2$  in the equation (2)). Thus, by simulating the dynamics of the output governed by the equation (2), we validated that such a simple incoherent feedforward loop is sufficient to produce in-phase and perfectly out-of-phase oscillations.

#### **2.4 Simulation results predict the role of AC in driving the in-phase behavior and decreasing time delay for perfectly out-of-phase behavior**

Since the above analyses for a simple incoherent feedforward loop suggest the role of AC\* in controlling the phase behavior of  $Ca^{2+}$ -cAMP, we tested whether the AC activity in the 3D reaction-diffusion model also plays a similar role. Therefore, we decreased the maximal concentration of AC to 75%, 50%, and 25% of the original value, and then simulated the 3D reaction-diffusion model (Figure 5A-C). We found that the in-phase behavior on AKAP/AC nanodomains and perfectly out-of-phase behavior outside AKAP/AC nanodomains still exist for the 75% and 50% cases (Figure 5A-B and D), but only perfectly out-of-phase behavior appears for the 25% case (Figure 5C-D). These results are consistent with the effect of activation strength  $v$ , because a small value of  $v$  usually leads to out-

of-phase behavior. In addition to the effect of AC activity on the phase difference between  $\text{Ca}^{2+}$  and cAMP, AC activity also influences the time delay for the perfectly out-of-phase behavior, that is, the higher the AC activity is, the shorter the time delay is (Figure 5E).

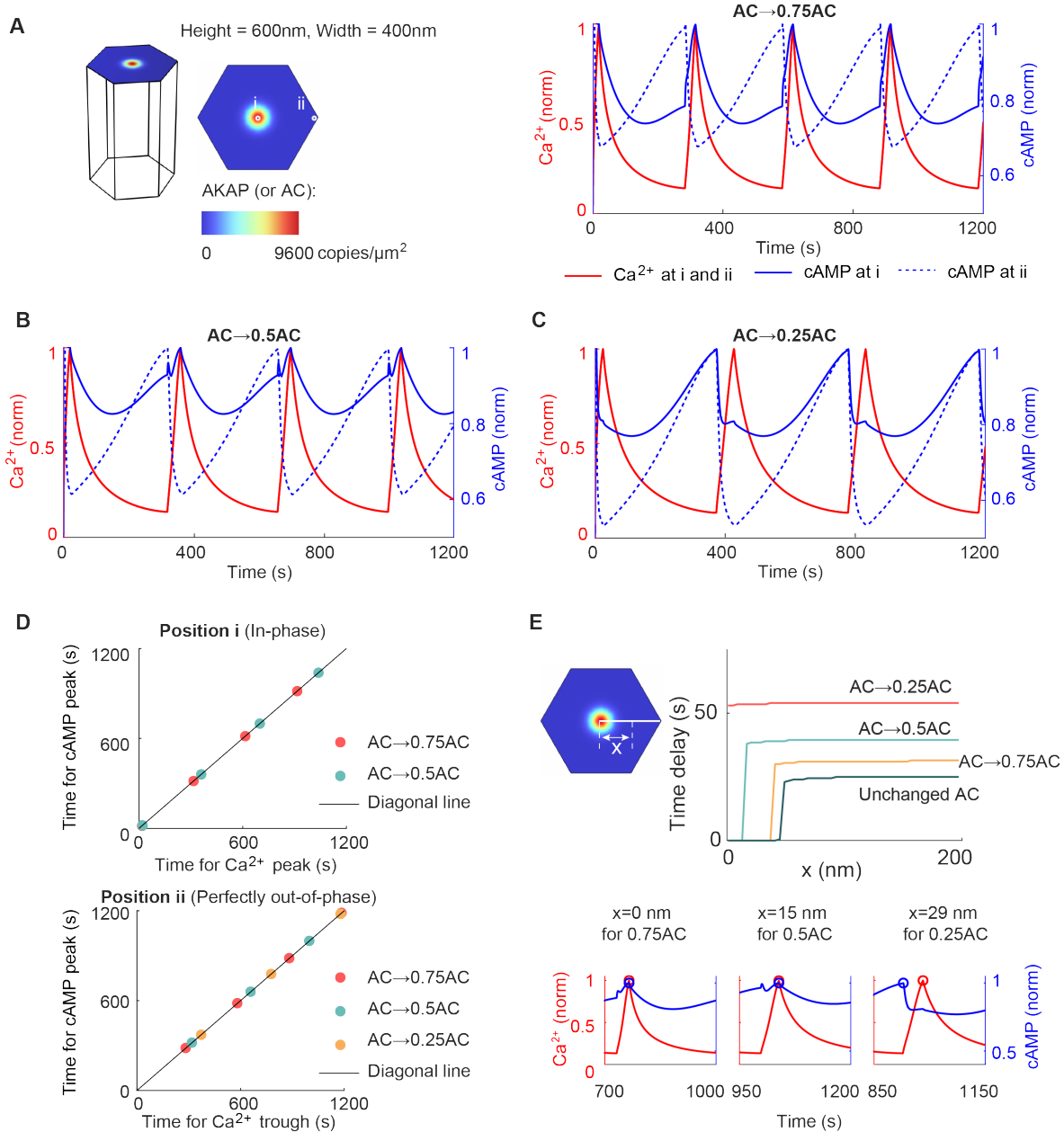


**Figure 5: Simulation results predict the role of AC in driving the in-phase behavior and decreasing time delay for perfectly out-of-phase behavior.** (A-C) The dynamics of  $\text{Ca}^{2+}$  and cAMP at different locations when the AC level is varied. The AC concentration is 75% (A), 50% (B), and 25% (C) of the original value. (D) The in-phase and perfectly out-of-phase cAMP behavior in (A-C). (E) The time delay of peaks between  $\text{Ca}^{2+}$  and cAMP as a function of the distance  $x$  in (A-B). The  $x$  has the same definition as that in Figure 2B.

## 2.5 Cellular compartment size determines the time delay for the perfectly out-of-phase $\text{Ca}^{2+}$ -cAMP oscillation

Having analyzed the biochemical mechanisms that regulate the  $\text{Ca}^{2+}$ -cAMP phase difference, we next turn our attention to the biophysical properties that may regulate the spatiotemporal dynamics of cell signaling, including the compartment size to investigate how it influences this phase difference. First, we tested the effect of the compartment size by doubling the height (Figure 6A), doubling the width (Figure 6B), or doubling both the height and width (Figure 6C). This effectively changes the surface-to-volume ratio of the cellular compartment. Similar to the original compartment (Figure 2A), these large compartments all lead to in-phase cAMP oscillation on the AKAP/AC nanodomains and perfectly out-of-phase cAMP oscillation outside the AKAP/AC nanodomains (Figure 6A-D). However, the time delay for the perfectly out-of-phase behavior differs (Figure 6E): it is near 25 seconds for the original compartment (black dashed line in Figure 6E), 50 seconds for the compartments with the double width or double height (red and cyan lines in Figure 6E), and 120 seconds for the compartment with double width and height (yellow line in Figure 6E). The compartment with the double width and that with double height have different sizes but similar time delay, indicating that the compartment size cannot monotonically determine the time delay (also see Figure S1). Nevertheless, by comparing these large compartments with the original compartment, we predict that the time delay for the perfectly out-of-phase cAMP oscillation depends on the compartment size, and the large compartment size tends to induce a long time delay.

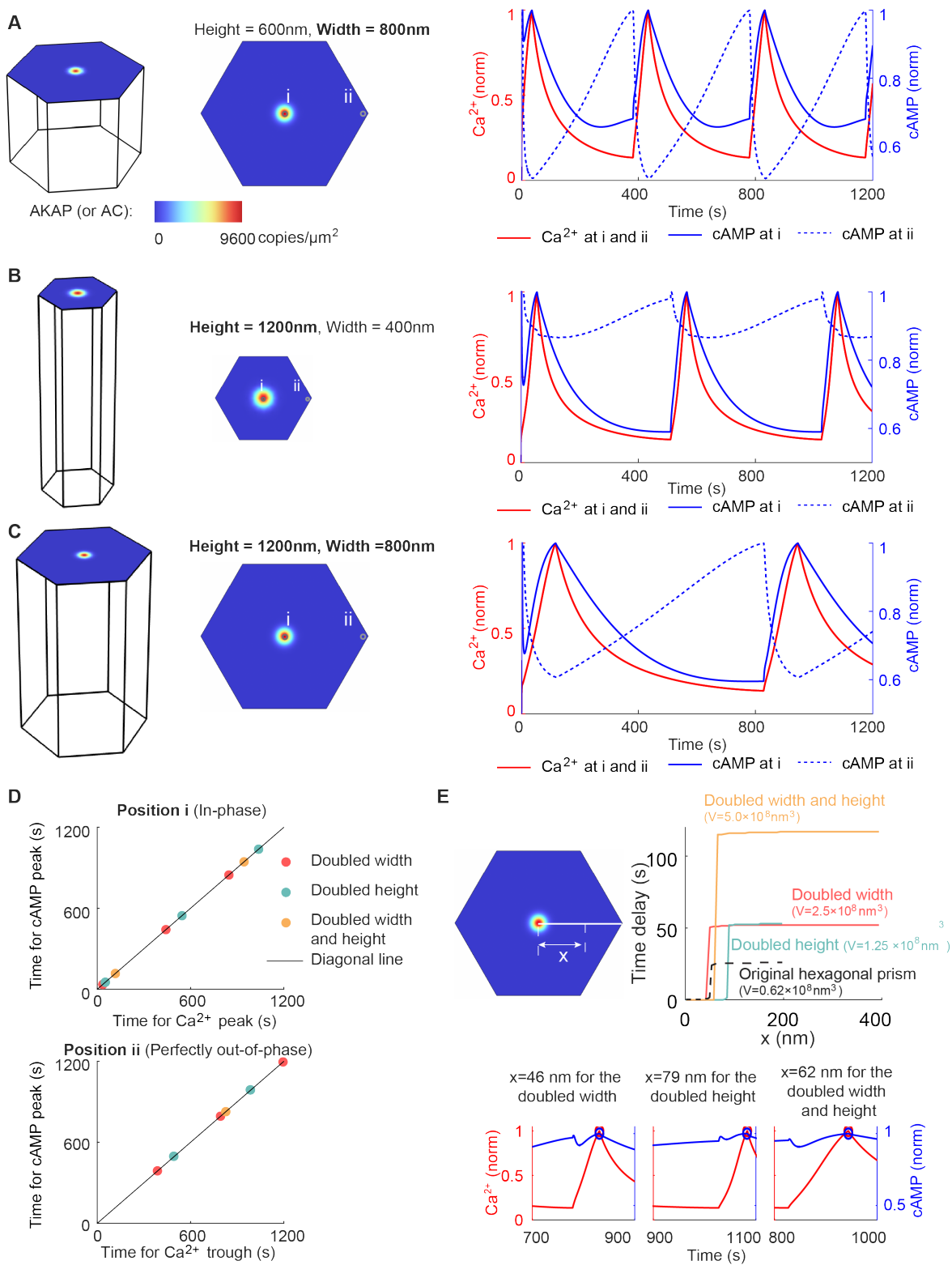


Figure 6: **Cellular compartment size determines the time delay for the perfectly out-of-phase Ca<sup>2+</sup>-cAMP oscillation.** (A) The Ca<sup>2+</sup> and cAMP dynamics for a double-width compartment. Dynamics on the AKAP/AC nanodomain (i) and at the edge of the compartment (ii) are shown. (B-C) Same plots as (A) except the compartment size. The compartment is doubled in height in (B) and doubled in both height and width in (C). (D) The in-phase and perfectly out-of-phase oscillations in (A-C). (E) The time delay in (A-C) as a function of the distance  $x$  to the nanodomain. The lower panel shows the magnified view of the Ca<sup>2+</sup> and cAMP dynamics when  $x$  is close to the critical value, which is defined as the time when the transition of time delay occurs.

## 2.6 AKAP/AC nanodomain formation can be explained by Turing patterns

Thus far, we focused on the impact of preexisting nanodomains. We next investigated the conditions that could lead to the formation of nanodomains. Inspired by work done by others on the formation of membrane receptor nanodomains [48, 57, 58, 59, 60], we focused on a Turing model with steric interactions [48]. This model is summarized as follows (Figure 1E):

$$\begin{cases} \frac{\partial r}{\partial t} = -b\left(r - \frac{s}{\bar{s}} \frac{1-r-s}{1-\bar{r}-\bar{s}} \bar{r}\right) - m_1 \frac{1-r-s}{1-\bar{r}-\bar{s}} (r - \bar{r}) + m_2 \frac{1-r-s}{1-\bar{r}-\bar{s}} \frac{r}{\bar{r}} (s - \bar{s}) \\ \quad + D_r \nabla[(1-s)\nabla r + r\nabla s] \\ \frac{\partial s}{\partial t} = -\beta\left(s - \frac{1-r-s}{1-\bar{r}-\bar{s}} \bar{s}\right) + \mu \frac{1-r-s}{1-\bar{r}-\bar{s}} \frac{s}{\bar{s}} (s - \bar{s}) + D_s \nabla[(1-r)\nabla s + s\nabla r]. \end{cases} \quad (3)$$

In the equation (3),  $r$  and  $s$  denote the normalized AC and AKAP concentration, respectively. AKAP works as a scaffold to recruit AC to cell membrane, and AC inhibits the recruitment of AKAP by steric repulsion similar to the model presented in [48].  $\bar{r}$  and  $\bar{s}$  are the value of  $r$  and  $s$  at homogeneous steady state.  $b$  and  $\beta$  are the unbinding rates of the AC and AKAP from the cell membrane, respectively;  $m_1$  and  $m_2$  are the binding rates of the AC to cell membrane caused by itself and the AKAP, respectively;  $\mu$  is the self-recruitment rate of AKAP;  $D_r$  and  $D_s$  are diffusion coefficients. The values of these kinetic parameters are listed in Table S6.

We simulated the above Turing model in a hexagonal domain of 800 nm for different combinations of kinetic parameters (Figure 7A). We found that three patterns arise: a homogeneous steady state where AC (denoted by  $r$ ) and AKAP (denoted by  $s$ ) are both uniformly distributed (lower left panel in Figure 7A), Turing pattern 1 where AC and AKAP are co-localized (lower middle panel in Figure 7A), and Turing pattern 2 where AC and AKAP repel each other (lower right panel in Figure 7A). We

found that the Turing pattern usually occurs when the ratio of the diffusion coefficient of AC to the diffusion coefficient of AKAP (i.e.,  $D_r/D_s$ ) is large (area in red and yellow in the upper left panel in Figure 7A), which is consistent with the condition of Turing instability. However, the large ratio leads to the transition from Turing pattern 1 to Turing pattern 2. Taken together with the fact that AC is co-localized with AKAP in MIN6  $\beta$  cells [32], our model predicts that the ratio of diffusion coefficients  $D_r/D_s$  is a critical determinant of nanodomain formation with Turing pattern 1. We note that while Turing pattern 2 is a mathematically admissible solution, its relevance to cell signaling is as yet unknown. Furthermore, colocalization and nanodomain formation are not sensitive to the unbinding rate of the AC (denoted by  $b$ ) but have a strict requirement on the unbinding rate of the AKAP, binding rate of the AC to cell membrane caused by AKAP, and the self-recruitment rate of AKAP (denoted by  $\beta$ ,  $m_2$ , and  $\mu$ , respectively) (upper middle and upper right panels in Figure 7A).

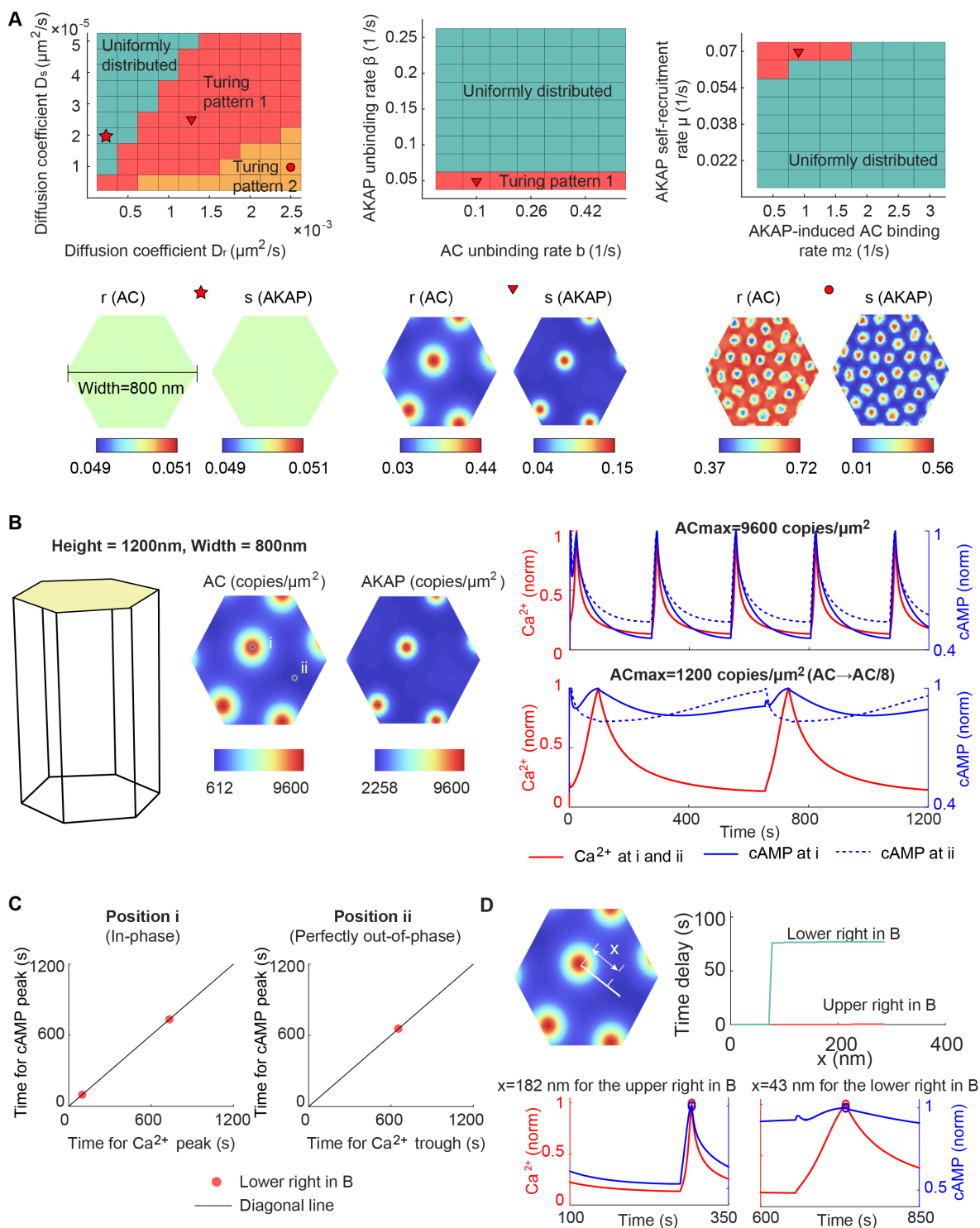


**Figure 7: AKAP/AC nanodomain formation can be explained by Turing patterns.** (A) The phase diagram of Turing pattern for parameters  $v_r$  and  $v_s$  (upper left panel),  $\beta$  and  $b$  (upper middle panel), and  $m_2$  and  $\mu$  (upper right panel). Three patterns occur in the parameter space: the first is that the AC (denoted by  $r$ ) and AKAP (denoted by  $s$ ) are uniformly distributed; the second is the Turing pattern where the AKAP and AC are co-localized, which is denoted as Turing pattern 1; the third is also a Turing pattern but the AC level is high outside the AKAP cluster, which is referred to as Turing pattern 2. Typical distributions of AC and AKAP for these three types of pattern are shown in lower panels. The marker over the plot indicates the value of  $D_r$ ,  $D_s$ ,  $\beta$ ,  $b$ ,  $m_2$  and  $\mu$ . (B) The dynamics of  $\text{Ca}^{2+}$  and cAMP on (i) or outside AKAP/AC nanodomains (ii) when initial conditions of AC and AKAP are re-scaled from the lower middle panel in (A). When the maximal concentration of AC is same as that in Figure 6, the cAMP oscillates in phase with  $\text{Ca}^{2+}$  on and outside AKAP/AC nanodomains (upper right panel); when the AC level is one eighth of that in Figures 6, the cAMP oscillates in phase with  $\text{Ca}^{2+}$  on AKAP/AC nanodomains but out of phase with  $\text{Ca}^{2+}$  outside AKAP/AC nanodomains (lower right panel). (C) The in-phase and perfectly out-of-phase oscillations in (B). (D) The time delay in (B) as a function of the distance  $x$  to the center of AKAP/AC nanodomains.

We next investigated the phase behavior of  $\text{Ca}^{2+}$ -cAMP in these Turing pattern-based nanodomains. To do so, we used the Turing pattern in the lower middle panel in Figure 7A as the initial condition of AKAP/AC nanodomains in the system described by equation (S1) (left panel in Figure 7B; also see Section S4). In this case, we have experimentally informed patterns but do not know the concentrations of the species. Since the simple ODE model indicates biochemical activity is important, we used the concentration of AC as free parameters and conducted a parameter variation. During this parameter variation, the largest concentration of AKAP on the AKAP/AC nanodomain was fixed to 9600 copies  $/\mu\text{m}^2$  to ensure the consistency with simulation results in Figure 6. The first rescaling set the largest concentration of AC on the AKAP/AC nanodomain to 9600 copies  $/\mu\text{m}^2$ , which was used in Figure 6. Given this re-scaling, the in-phase cAMP oscillation exists not only on AKAP/AC nanodomains but also outside AKAP/AC nanodomains (upper right panel in Figure 7B). This is consistent with our previous finding of in-phase oscillations on the AKAP/AC nanodomain but not consistent with the perfectly out-of-phase oscillations outside the AKAP/AC nanodomain. Next, we decreased the concentration of AC to 12.5% of the previous value, and thus the largest AC concentration on



the AKAP/AC nanodomain becomes 1200 copies  $/\mu\text{m}^2$ . We found the emergence of perfectly out-of-phase cAMP oscillation outside AKAP/AC nanodomains (lower right panel in Figure 7B; Figure 7C-D). Thus, our model predicted that Turing pattern 1 combined with the ratio of AC to AKAP is critical in regulating the phase behavior of  $\text{Ca}^{2+}$ -cAMP. This prediction demonstrates the importance of both pattern formation and biochemical activity in  $\text{Ca}^{2+}$ -cAMP oscillation.

## 2.7 Prediction of the time delay from a realistic distribution of AKAP/AC nanodomains

Finally, we extended our analysis to the realistic distribution of AKAP/AC nanodomains from AC8 STORM data in [32]. This analysis allows us to relax the previous assumptions of the nanodomains as either Gaussian distribution or Turing pattern and test our models in experimentally observed nanodomain distributions. To do this, we selected one square area with a length of 1000 nm from the STORM data (left and middle panels in Figure 8A); and then smoothed the STORM data in the square area by convoluting with a Gaussian function whose FWHM (full width at half maximum) is 60 nm (right panel in Figure 8A). After these two processes, we obtained a smooth distribution of AC8 on a square area with a length of 1000 nm. Next, the AC8 distribution in a hexagonal region denoted by the white dashed line (right panel in Figure 8A) is used as the initial distribution of AC in our simulations. Similar to the case with Turing pattern-based AKAP/AC nanodomain, the realistic concentration of AC is unknown. As suggested by the model results with Turing pattern-based AKAP/AC nanodomain, the AC activity plays an important role in the phase behavior of  $\text{Ca}^{2+}$ -cAMP, and thus we also tested two values of rescaled AC here: the first is that the largest value of AC concentration on the AKAP/AC nanodomain is rescaled to 9600 copies/ $\mu\text{m}^2$  (upper right panel in Figure 8B), and the second is 4800 copies/ $\mu\text{m}^2$  (lower right panel in Figure 8B). Additionally, the initial distribution of AKAP is always rescaled to ensure the highest concentration on AKAP/AC nanodomain of 9600 copies/ $\mu\text{m}^2$ .

The two different rescalings of the AC activity result in distinct phase behavior. The first rescaling shows in-phase  $\text{Ca}^{2+}$ -cAMP oscillation on and outside the AKAP/AC nanodomains (upper right panel in Figure 8B). For the second rescaling of 4800 copies/ $\mu\text{m}^2$ , the in-phase cAMP oscillation on AKAP/AC nanodomains and perfectly out-of-phase cAMP oscillation outside the AKAP/AC nanodomains arise again (lower right panel in Figure 8B; Figure 8C-D). Therefore, our model predicts that the AC activity is essential for the phase difference between  $\text{Ca}^{2+}$ -cAMP even for a realistic distribution of AKAP/AC nanodomains.

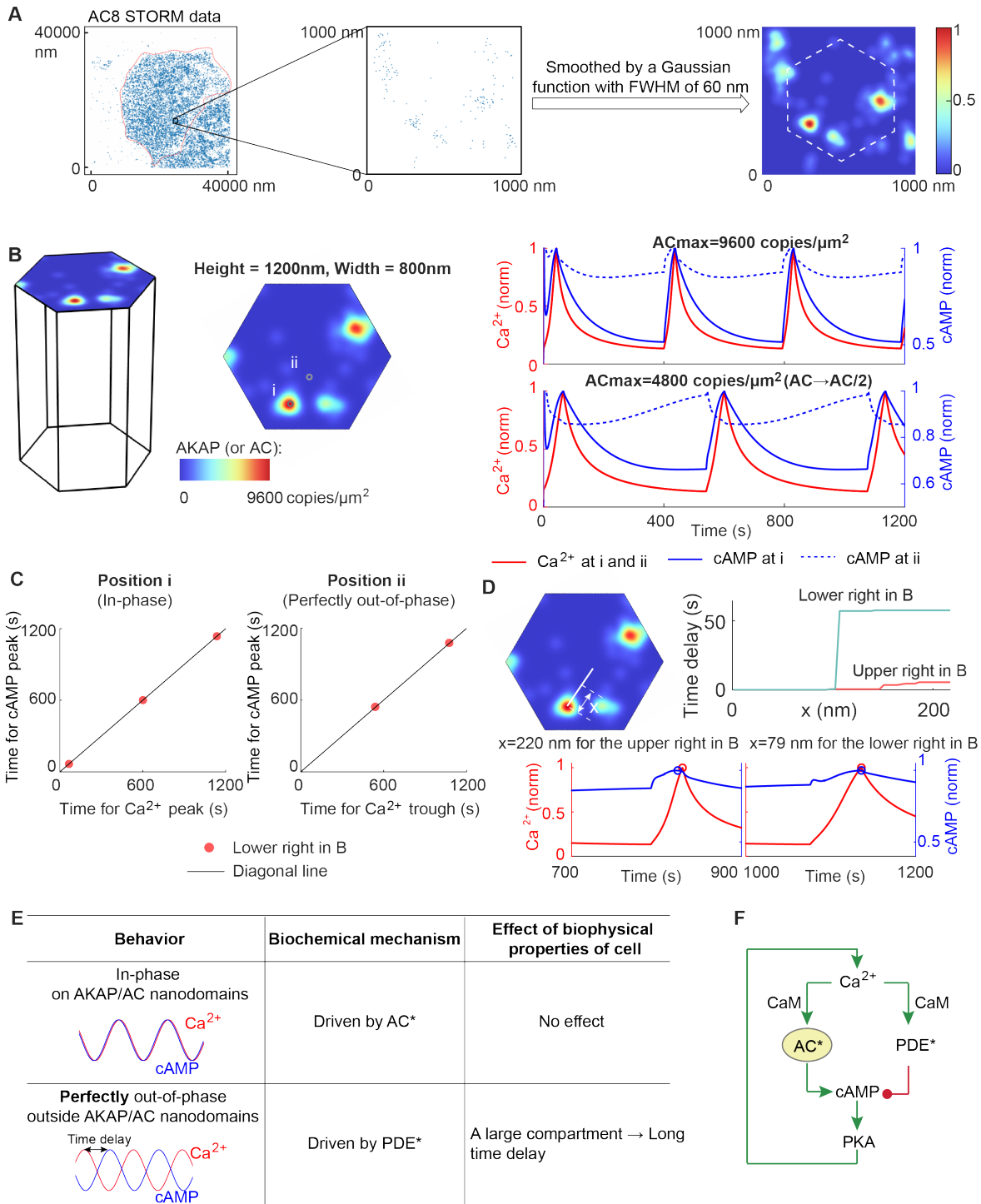


**Figure 8: Prediction of the time delay from a realistic distribution of AKAP/AC nanodomains.**

(A) Extraction of AC8 data from STORM image. The AC8 STORM data (left panel) is from [32], where the red dashed line indicates the boundary of a single cell. We selected an area with 1000 nm length and 10000 nm width (middle panel), then smoothed the STORM data in this small area by a Gaussian function with FWHM (full width at half maximum) of 60 nm, and finally obtained a smooth distribution of AC8 on the small area (right panel). We chose a hexagon indicated by the white dashed line as the distribution of AC in the following simulations. (B) The dynamics of  $\text{Ca}^{2+}$  and cAMP on the AKAP/AC nanodomain (i) and outside the AKAP/AC nanodomain (ii) when the initial distribution of AC is from (A). The initial distribution of AKAP is set to be the same as that of AC. Two cases are studied: the AC has the same maximal values as before (i.e., 9600 copies/ $\mu\text{m}^2$ ) (upper right panel); the AC level is halved (lower right panel). (C) The in-phase and perfectly out-of-phase oscillations in the lower right panel in (B). (D) The time delay as a function of the distance to the AKAP/AC nanodomain. (E) Summary of  $\text{Ca}^{2+}$ -cAMP oscillation, underlying biochemical mechanisms, and the effect of the biophysical properties of the cell. (F) The core motif of the  $\text{Ca}^{2+}$ /cAMP circuit – incoherent feedforward loop from  $\text{Ca}^{2+}$  to cAMP and the feedback from cAMP to  $\text{Ca}^{2+}$ .

### 3 Discussion

Signaling nanodomains and biomolecular condensates are ubiquitous within the cell. They regulate signaling transduction pathways by sequestering biochemical reactions. However, how these signaling aggregates precisely regulate intracellular pathways remains elusive, especially when taking the nonuniform size and distribution of these signaling aggregates in the cell into consideration. Here, we looked at the intersection of AKAP/AC nanodomain and the  $\text{Ca}^{2+}$ /cAMP pathway in detail and studied the underlying biochemical mechanisms and potential biophysical effects.

We developed a 3D reaction-diffusion model and different types of preexisting AKAP/AC nanodomains to study how AC and PDE activities, compartment size, and pattern of AKAP/AC nanodomains affect the phase shift between  $\text{Ca}^{2+}$  and cAMP oscillation. Through simulating the 3D reaction-diffusion model with a Gaussian distribution-modeled AKAP/AC nanodomain, we revealed the paradoxical role of AC and PDE: active AC and active PDE drive in-phase oscillation on AKAP/AC

nanodomains and out-of-phase oscillation outside AKAP/AC nanodomains, respectively (first and second columns in Figure 8E). It should be noted that the out-of-phase oscillation is perfect, which is validated by the close match of  $\text{Ca}^{2+}$  trough time and cAMP peak time in the experiment. Such paradoxical role of AC and PDE in regulating the phase shift between  $\text{Ca}^{2+}$  and cAMP can be explained by a simple incoherent feedforward loop and predicted by varying AC activity in the 3D reaction-diffusion model. Furthermore, the important role of AC in regulating phase delay between  $\text{Ca}^{2+}$  and cAMP has been demonstrated by knocking down AC, overexpressing AC, or disturbing the interaction between AKAP and AC (Figure 2(d-e) and Figure 5(b) in [32]). Moreover, these in-phase and perfectly out-of-phase behaviors persist in most cases, but the time delay for the perfectly out-of-phase behavior depends on the compartment size (third column in Figure 8E). Furthermore, the simulation results with Turing pattern-based and AC STORM data-based AKAP/AC nanodomains predicted the important role of nanodomain pattern and AC activity in coordinating the phase between  $\text{Ca}^{2+}$  and cAMP.

Interestingly, we found that the phase shift between  $\text{Ca}^{2+}$  and cAMP is controlled by an incoherent feedforward loop: the activating  $\text{Ca}^{2+}$ -AC-cAMP pathway and the inhibiting  $\text{Ca}^{2+}$ -PDE-cAMP pathway (Figure 8F). Although the cAMP can regulate the  $\text{Ca}^{2+}$  level by a feedback loop through PKA (Figure 8F), it seems that the difference in oscillatory dynamics of cAMP at distinct cellular locations does not result in diverse  $\text{Ca}^{2+}$  dynamics due to the fast diffusion of  $\text{Ca}^{2+}$ . Several well-known biological functions of the incoherent feedforward loop include achieving adaptation [54, 55, 61], regulating structural plasticity [56], processing oscillation [50], detecting fold-change [52], generating non-monotonic gene input functions [51], and facilitating adaptive tuning of gene expression [53], but the phase regulation of second messengers is first discovered in this work to our knowledge. Since the cell decodes information involved in second messengers to regulate gene transcription [14, 31, 62], the incoherent feedforward loop may play a broad role in gene expression.

The exploration of mechanisms of in-phase and perfectly out-of-phase behavior in this work may help to understand the synchronization in oscillatory systems. The synchronization, which is widely observed in circadian clocks [63], long-term memory [64, 65], and collective behavior in cell populations [66, 67], is referred to as the locked phase for several interacting biological oscillators. Depending on the phase difference, the synchronization includes in-phase synchronization, anti-phase (or perfectly out-of-phase) synchronization, and synchronization with an arbitrary phase shift. Therefore, if we regarded the  $\text{Ca}^{2+}$  and cAMP as two biological oscillators, their in-phase and perfectly

out-of-phase behavior are two types of synchronization. Our numerical results suggest that improving the activation strength from one oscillator to the other ( $v$  in Equation (2)) can only lead to a sudden change from perfectly out-of-phase synchronization to in-phase synchronization rather than a continuous change. Furthermore, a continuous change in phase difference can be achieved by tuning the basal inhibition rate of the downstream oscillator ( $k_2$  in the main text), and the large rate results in the in-phase or perfectly out-of-phase synchronization.

Our work demonstrates the role of biophysical properties of the cell in  $\text{Ca}^{2+}$ -cAMP oscillation, which is another evidence that the biophysical properties of cells encode the signaling information. One important biophysical property of cells is cell shape. For example, cell aspect ratio affects cytosolic calcium levels in vascular smooth muscle cells [68]; the structure and the shape of the dendrite spine regulate AMPAR dynamics and energy landscape [69, 70]; the cell eccentricity encodes the information of growth factor receptor pathways [71]. While most studies focused on the change in the increase or decrease of intracellular signaling levels, our work observed the change in period and phase for oscillatory signaling molecules. Apart from the cell shape, the distribution of AKAP/AC nanodomains also plays a role in  $\text{Ca}^{2+}$ -cAMP oscillation. This result implies the importance of the signaling hubs, which has been revealed in many biological systems [72, 73, 74, 75]. The major function of signaling hubs is to sequester the chemical reactions to ensure their occurrence in the right locations, and AKAP/AC nanodomains also exhibit similar behavior: the activation of AC can only happen on AKAP/AC nanodomains, and thus guarantees the high value of cAMP on AKAP/AC nanodomains.

The phase behavior of  $\text{Ca}^{2+}$ -cAMP in pancreatic  $\beta$  cell may be crucial to insulin secretion. The cAMP not only affects the  $\text{Ca}^{2+}$  level as modeled in this work but also regulates PKA and guanine exchange factor Epac, two types of signaling molecules that contribute to secretory granule trafficking and exocytosis. On the one hand, both PKA and Epac improve the mobilization of secretory granules, resulting in fast replenishment of readily releasable granules [76, 77, 78]. On the other hand, several proteins involved in the exocytosis process have been identified as substrates of PKA or interacted with Epac, such as SNAP-25 and Snapin [79, 80, 81, 82]. Moreover, AKAP nanodomains can anchor both PKA and Epac [83, 84], and thus may drive the oscillation of PKA and Epac during pulsatile insulin secretion.

The AKAP/AC nanodomains mediate the phase difference between  $\text{Ca}^{2+}$  and cAMP. Such nanodomains have been extensively found in the intracellular space as well as biomolecular condensates

[85, 86, 87, 88]. These signaling nanodomains and biomolecular condensates are able to directly regulate cellular processes, and dysregulations of these complexes are likely indicated as potential drivers of oncogenic activity. For example, the tumor suppressor SPOP (speckle-type POZ protein) granules are disrupted in the presence of SPOP mutations that promote prostate cancer progression [89, 90]; the stress granules, which are composed of mRNA transcripts, RNA-binding proteins, and translation machinery to prevent cell apoptosis from stressful conditions, are markedly upregulated in cancer cells, resulting in more stress-resistant cancer cells [91, 92]; the promyelocytic leukemia (PML) nuclear bodies have been found to contribute to the telomere lengthening in cancer cells, thus improving the replicative ability of cancer cells [93, 94]; the flat clathrin lattice (FCL) is located on the cell membrane, providing sustained signaling hubs for epidermal growth factor receptor (EGFR), and the disruption of FCL leads to a decreased level of active EGFR on the cell membrane [72].

In addition to its application in receptor nanodomains, the Turing model is commonly employed to understand mechanisms underlying a wide range of biological patterns such as sea shell patterns, hair follicle spacing, hydra regeneration, lung branching and digits formation [95, 96, 97, 98]. With a simple interaction network incorporating a short-range positive feedback and a long-range negative feedback (i.e., a slowly diffusing activator and a rapidly diffusing inhibitor), the Turing model is able to reproduce diverse spatial patterns. For example, a simple Turing reaction-diffusion model consisting of the phosphorylated and unphosphorylated species of Polo-like-kinase 4 (PLK4), is used to explain how mother centrioles break symmetry to generate a single daughter [99]. When taking the intrinsic noise into account, the stochastic version of Turing model can further relax parameter constraints such as the ratio of activator–inhibitor diffusion coefficients, which is validated in a synthetic bacterial population where the signaling molecules form a stochastic activator–inhibitor system [100].

Although we used the Turing model to explain the formation of AKAP/AC nanodomains, it is not the only one that can generate the pattern. For example, the particle-based model [57, 58, 59, 60], lattice model [101, 102], and Cahn–Hilliard equation [103, 104, 105] can also produce patterns. The Cahn–Hilliard equation is well-known as the model for phase separation, but recently it has been used to model the formation of nanodomains on cell membranes. We also note that the Turing pattern in this work is a qualitative match but not a quantitative one, since the size of Turing pattern was not fitted to experimental data. In addition to the limitation in choosing the patterning model, another limitation in our work is that we did not consider the existence of RI $\alpha$  (a subunit of PKA) condensates in the cytosol, which can accumulate cAMP locally [75]; future work is expected to

incorporate  $RI\alpha$  condensates to fill the knowledge gap. Another limitation is that we neglected the biological noise in the  $Ca^{2+}/cAMP$  circuit. Despite these limitations, our findings of  $Ca^{2+}$ -cAMP interacting through an incoherent feedforward loop to regulate their in and out-of-phase oscillations on AKAP/AC nanodomains sheds light on how spatial arrangement of molecules can regulate temporal dynamics of second messengers in different cellular locations.

## **4 Acknowledgments**

This work was supported by the National Institute of Health Grant R01 DK073368 (to J.Z.) and the Air Force Office of Scientific Research (AFOSR) Multidisciplinary University Research Initiative (MURI) Grant FA9550-18-1-0051 (to P.R.).

## **5 Author contributions**

P.R. and J.Z. conceived the study. L.Q. performed the simulations and analyses. M.G. and B.G. provided the original simulation code. B.T. provided the experimental data. L.Q., M.G., B.G., B.T., J.Z., and P.R. co-wrote the manuscript.

## References

- [1] J. A. Beavo and L. L. Brunton. Cyclic nucleotide research — still expanding after half a century. *Nature Reviews Molecular Cell Biology*, 3(9):710–717, 2002.
- [2] I. Drago, D. D. Stefani, R. Rizzuto, and T. Pozzan. Mitochondrial  $\text{Ca}^{2+}$  uptake contributes to buffering cytoplasmic  $\text{Ca}^{2+}$  peaks in cardiomyocytes. *Proceedings of the National Academy of Sciences*, 109(32):12986–12991, 2012.
- [3] C. Giorgi, S. Marchi, and P. Pinton. The machineries, regulation and cellular functions of mitochondrial calcium. *Nature Reviews Molecular Cell Biology*, 19(11):713–730, 2018.
- [4] D. E. Clapham. Calcium signaling. *Cell*, 131(6):1047–1058, 2007.
- [5] E. Kwok, S. C. Otto, P. Khuu, A. P. Carpenter, S. J. Coddling, P. N. Reardon, J. Vanegas, T. M. Kumar, C. J. Kuykendall, R. A. Mehl, J. Baio, and C. P. Johnson. The dysferlin C2A domain binds PI(4,5)P2 and penetrates membranes. *Journal of Molecular Biology*, 435(17):168193, 2023.
- [6] J. K. Williams, J. M. Ngo, I. M. Lehman, and R. Schekman. Annexin A6 mediates calcium-dependent exosome secretion during plasma membrane repair. *eLife*, 12:e86556, 2023.
- [7] C. H. Serezani, M. N. Ballinger, D. M. Aronoff, and M. Peters-Golden. Cyclic AMP. *American Journal of Respiratory Cell and Molecular Biology*, 39(2):127–132, 2008. PMID: 18323530.
- [8] P. Sassone-Corsi. The cyclic AMP pathway. *Cold Spring Harbor Perspectives in Biology*, 4(12), 2012.
- [9] H. Zhang, Q. Kong, J. Wang, Y. Jiang, and H. Hua. Complex roles of cAMP–PKA–CREB signaling in cancer. *Experimental Hematology & Oncology*, 9(1):32, 2020.
- [10] M. Massimi, S. Cardarelli, F. Galli, M. F. Giardi, F. Ragusa, N. Panera, B. Cinque, M. G. Cifone, S. Biagioni, and M. Giorgi. Increase of intracellular cyclic AMP by PDE4 inhibitors affects HepG2 cell cycle progression and survival. *Journal of Cellular Biochemistry*, 118(6):1401–1411, 2017.



- [11] T. C. Chen, D. R. Hinton, R. Zidovetzki, and F. M. Hofman. Up-regulation of the cAMP/PKA pathway inhibits proliferation, induces differentiation, and leads to apoptosis in malignant gliomas. *Laboratory investigation; a journal of technical methods and pathology*, 78 2:165–74, 1998.
- [12] A. B. Parekh. Decoding cytosolic Ca<sup>2+</sup> oscillations. *Trends in Biochemical Sciences*, 36(2):78–87, 2011.
- [13] M. J. Berridge, M. D. Bootman, and P. Lipp. Calcium - a life and death signal. *Nature*, 395(6703):645–648, 1998.
- [14] E. Smedler and P. Uhlén. Frequency decoding of calcium oscillations. *Biochimica et Biophysica Acta (BBA) - General Subjects*, 1840(3):964–969, 2014.
- [15] R. E. Dolmetsch, K. Xu, and R. S. Lewis. Calcium oscillations increase the efficiency and specificity of gene expression. *Nature*, 392(6679):933–936, 1998.
- [16] M. Zaccolo, A. Zerio, and M. J. Lobo. Subcellular organization of the cAMP signaling pathway. *Pharmacological Reviews*, 73(1):278–309, 2021.
- [17] D. Calebiro and I. Maiellaro. cAMP signaling microdomains and their observation by optical methods. *Frontiers in cellular neuroscience*, 8:350, 2014.
- [18] O. H. Petersen. Calcium signal compartmentalization. *Biological Research*, 35:177 – 182, 2002.
- [19] A. J. Laude and A. W. M. Simpson. Compartmentalized signalling: Ca<sup>2+</sup> compartments, microdomains and the many facets of Ca<sup>2+</sup> signalling. *The FEBS Journal*, 276(7):1800–1816, 2009.
- [20] R. Dolmetsch. Excitation-transcription coupling: Signaling by ion channels to the nucleus. *Science's STKE*, 2003(166):pe4–pe4, 2003.
- [21] R. Rizzuto and T. Pozzan. Microdomains of intracellular Ca<sup>2+</sup>: Molecular determinants and functional consequences. *Physiological Reviews*, 86(1):369–408, 2006. PMID: 16371601.

- [22] C. Giorgi, D. De Stefani, A. Bononi, R. Rizzuto, and P. Pinton. Structural and functional link between the mitochondrial network and the endoplasmic reticulum. *The International Journal of Biochemistry and Cell Biology*, 41(10):1817–1827, 2009. Mitochondrial Dynamics and Function in Biology and Medicine.
- [23] G. Santulli, G. Pagano, C. Sardu, W. Xie, S. Reiken, S. L. D’Ascia, M. Cannone, N. Marziliano, B. Trimarco, T. A. Guise, A. Lacampagne, and A. R. Marks. Calcium release channel RyR2 regulates insulin release and glucose homeostasis. *The Journal of Clinical Investigation*, 125(5):1968–1978, 2015.
- [24] S. Kammerer, L. L. Burns-Hamuro, Y. Ma, S. C. Hamon, J. M. Cànaves, M. M. Shi, M. R. Nelson, C. F. Sing, C. R. Cantor, S. S. Taylor, and A. Braun. Amino acid variant in the kinase binding domain of dual-specific a kinase-anchoring protein 2: A disease susceptibility polymorphism. *Proceedings of the National Academy of Sciences*, 100(7):4066–4071, 2003.
- [25] V. O. Nikolaev, A. Moshkov, A. R. Lyon, M. Miragoli, P. Novak, H. Paur, M. J. Lohse, Y. E. Korchev, S. E. Harding, and J. Gorelik.  $\beta_2$ -adrenergic receptor redistribution in heart failure changes camp compartmentation. *Science*, 327(5973):1653–1657, 2010.
- [26] M. Wirtenberger, J. Schmutzhard, K. Hemminki, A. Meindl, C. Sutter, R. K. Schmutzler, B. Wappenschmidt, M. Kiechle, N. Arnold, B. H. Weber, D. Niederacher, C. R. Bartram, and B. Burwinkel. The functional genetic variant Ile 646 Val located in the kinase binding domain of the A-kinase anchoring protein 10 is associated with familial breast cancer. *Carcinogenesis*, 28(2):423–426, 2007.
- [27] J. K. Millar, B. S. Pickard, S. Mackie, R. James, S. Christie, S. R. Buchanan, M. P. Malloy, J. E. Chubb, E. Huston, G. S. Baillie, P. A. Thomson, E. V. Hill, N. J. Brandon, J.-C. Rain, L. M. Camargo, P. J. Whiting, M. D. Houslay, D. H. R. Blackwood, W. J. Muir, and D. J. Porteous. DISC1 and PDE4B are interacting genetic factors in schizophrenia that regulate camp signaling. *Science*, 310(5751):1187–1191, 2005.
- [28] L. Pasti, A. Volterra, T. Pozzan, and G. Carmignoto. Intracellular calcium oscillations in astrocytes: A highly plastic, bidirectional form of communication between neurons and astrocytes in situ. *Journal of Neuroscience*, 17(20):7817–7830, 1997.

- [29] K. L. Eckel-Mahan, T. Phan, S. Han, H. Wang, G. C.-K. Chan, Z. S. Scheiner, and D. R. Storm. Circadian oscillation of hippocampal MAPK activity and cAMP: implications for memory persistence. *Nature Neuroscience*, 11(9):1074–1082, 2008.
- [30] R. C. Addis, J. L. Ifkovits, F. Pinto, L. D. Kellam, P. Estes, S. Rentschler, N. Christoforou, J. A. Epstein, and J. D. Gearhart. Optimization of direct fibroblast reprogramming to cardiomyocytes using calcium activity as a functional measure of success. *Journal of Molecular and Cellular Cardiology*, 60:97–106, 2013.
- [31] O. Dyachok, Y. Isakov, J. S agertorp, and A. Tengholm. Oscillations of cyclic AMP in hormone-stimulated insulin-secreting  $\beta$ -cells. *Nature*, 439(7074):349–352, 2006.
- [32] B. Tenner, M. Getz, B. L. Ross, D. Ohadi, S. Mehta, P. Rangamani, and J. Zhang. Spatially compartmentalized phase regulation in the  $\text{Ca}^{2+}$ –cAMP–PKA oscillatory circuit. *Biophysical Journal*, 118(3):175a, 2020.
- [33] F. Siso-Nadal, J. J. Fox, S. A. Laporte, T. E. H ebert, and P. S. Swain. Cross-talk between signaling pathways can generate robust oscillations in calcium and cAMP. *PLOS ONE*, 4(10):1–10, 2009.
- [34] G. Dupont, L. Combettes, G. S. Bird, and J. W. Putney. Calcium oscillations. *Cold Spring Harbor Perspectives in Biology*, 3(3), 2011.
- [35] J. Sneyd, J. M. Han, L. Wang, J. Chen, X. Yang, A. Tanimura, M. J. Sanderson, V. Kirk, and D. I. Yule. On the dynamical structure of calcium oscillations. *Proceedings of the National Academy of Sciences*, 114(7):1456–1461, 2017.
- [36] B. E. Peercy, A. S. Sherman, and R. Bertram. Modeling of glucose-induced cAMP oscillations in pancreatic  $\beta$  cells: cAMP rocks when metabolism rolls. *Biophysical Journal*, 109(2):439–449, 2015.
- [37] L. Qiao, Z.-B. Zhang, W. Zhao, P. Wei, and L. Zhang. Network design principle for robust oscillatory behaviors with respect to biological noise. *eLife*, 11:e76188, 2022.
- [38] D. Ohadi, D. L. Schmitt, B. Calabrese, S. Halpain, J. Zhang, and P. Rangamani. Computational

- modeling reveals frequency modulation of calcium–cAMP/PKA pathway in dendritic spines. *Biophysical Journal*, 117(10):1963–1980, 2019.
- [39] D. Ohadi and P. Rangamani. Geometric control of frequency modulation of cAMP oscillations due to calcium in dendritic spines. *Biophysical Journal*, 117(10):1981–1994, 2019.
- [40] A. I. Tarasov, F. Semplici, M. A. Ravier, E. A. Bellomo, T. J. Pullen, P. Gilon, I. Sekler, R. Rizzuto, and G. A. Rutter. The mitochondrial  $\text{Ca}^{2+}$  uniporter MCU is essential for glucose-induced ATP increases in pancreatic  $\beta$  cells. *PLOS ONE*, 7(7):1–12, 2012.
- [41] F. M. Ashcroft and P. Rorsman. Diabetes mellitus and the  $\beta$  cell: The last ten years. *Cell*, 148(6):1160–1171, 2012.
- [42] Z. Zhou and S. Mislser. Amperometric detection of quantal secretion from patch-clamped rat pancreatic  $\beta$ -cells. *Journal of Biological Chemistry*, 271(1):270–277, 1996.
- [43] A. Tomas, B. Jones, and C. Leech. New insights into  $\beta$ -cell GLP-1 receptor and cAMP signaling. *Journal of Molecular Biology*, 432(5):1347–1366, 2020. Islet Biology in Type 2 diabetes.
- [44] H. Dou, C. Wang, X. Wu, L. Yao, X. Zhang, S. Teng, H. Xu, B. Liu, Q. Wu, Q. Zhang, M. Hu, Y. Wang, L. Wang, Y. Wu, S. Shang, X. Kang, L. Zheng, J. Zhang, M. Raoux, J. Lang, Q. Li, J. Su, X. Yu, L. Chen, and Z. Zhou. Calcium influx activates adenylyl cyclase 8 for sustained insulin secretion in rat pancreatic beta cells. *Diabetologia*, 58(2):324–333, 2015.
- [45] A. Tengholm and E. Gylfe. cAMP signalling in insulin and glucagon secretion. *Diabetes, Obesity and Metabolism*, 19(S1):42–53, 2017.
- [46] Q. Ni, A. Ganesan, N.-N. Aye-Han, X. Gao, M. D. Allen, A. Levchenko, and J. Zhang. Signaling diversity of PKA achieved via a  $\text{Ca}^{2+}$ -cAMP–PKA oscillatory circuit. *Nature chemical biology*, 7(1):34–40, 2011.
- [47] M. G. Gold, F. Stengel, P. J. Nygren, C. R. Weisbrod, J. E. Bruce, C. V. Robinson, D. Barford, and J. D. Scott. Architecture and dynamics of an a-kinase anchoring protein 79 (akap79) signaling complex. *Proceedings of the National Academy of Sciences*, 108(16):6426–6431, 2011.

- [48] C. A. Haselwandter, M. Calamai, M. Kardar, A. Triller, and R. A. da Silveira. Formation and stability of synaptic receptor domains. *Physical Review Letters*, 106(23):238104, 2011.
- [49] U. Alon. *An introduction to systems biology: design principles of biological circuits*. CRC press, 2019.
- [50] C. Zhang, R. Tsoi, F. Wu, and L. You. Processing oscillatory signals by incoherent feedforward loops. *PLOS Computational Biology*, 12(9):1–16, 2016.
- [51] S. Kaplan, A. Bren, E. Dekel, and U. Alon. The incoherent feed-forward loop can generate non-monotonic input functions for genes. *Molecular Systems Biology*, 4(1):203, 2008.
- [52] L. Goentoro, O. Shoval, M. W. Kirschner, and U. Alon. The incoherent feedforward loop can provide fold-change detection in gene regulation. *Molecular Cell*, 36(5):894–899, 2009.
- [53] J. Hong, N. Brandt, F. Abdul-Rahman, A. Yang, T. Hughes, and D. Gresham. An incoherent feedforward loop facilitates adaptive tuning of gene expression. *eLife*, 7:e32323, 2018.
- [54] L. Qiao, W. Zhao, C. Tang, Q. Nie, and L. Zhang. Network topologies that can achieve dual function of adaptation and noise attenuation. *Cell systems*, 9(3):271–285, 2019.
- [55] W. Ma, A. Trusina, H. El-Samad, W. A. Lim, and C. Tang. Defining network topologies that can achieve biochemical adaptation. *Cell*, 138(4):760–773, 2009.
- [56] P. Rangamani, M. G. Levy, S. Khan, and G. Oster. Paradoxical signaling regulates structural plasticity in dendritic spines. *Proceedings of the National Academy of Sciences*, 113(36):E5298–E5307, 2016.
- [57] I. Palaia and A. Šarić. Controlling cluster size in 2D phase-separating binary mixtures with specific interactions. *The Journal of Chemical Physics*, 156(19):194902, 2022.
- [58] M. J. Varga, Y. Fu, S. Loggia, O. N. Yagorcu, and M. E. Johnson. Nerdss: A nonequilibrium simulator for multibody self-assembly at the cellular scale. *Biophysical Journal*, 118(12):3026–3040, 2020.
- [59] M. Pablo, S. A. Ramirez, and T. C. Elston. Particle-based simulations of polarity establishment reveal stochastic promotion of turing pattern formation. *PLOS Computational Biology*, 14(3):1–25, 2018.

- [60] A. Ullrich, M. A. Böhme, J. Schöneberg, H. Depner, S. J. Sigrist, and F. Noé. Dynamical organization of syntaxin-1A at the presynaptic active zone. *PLOS Computational Biology*, 11(9):1–22, 2015.
- [61] K. Takeda, D. Shao, M. Adler, P. G. Charest, W. F. Loomis, H. Levine, A. Groisman, W.-J. Rappel, and R. A. Firtel. Incoherent feedforward control governs adaptation of activated ras in a eukaryotic chemotaxis pathway. *Science Signaling*, 5(205):ra2–ra2, 2012.
- [62] R. Lewis. Calcium oscillations in T-cells: mechanisms and consequences for gene expression. *Biochemical Society Transactions*, 31(5):925–929, 2003.
- [63] S. J. Aton and E. D. Herzog. Come together, right. now: Synchronization of rhythms in a mammalian circadian clock. *Neuron*, 48(4):531–534, 2005.
- [64] S. Hanslmayr, T. Staudigl, and M.-C. Fellner. Oscillatory power decreases and long-term memory: the information via desynchronization hypothesis. *Frontiers in Human Neuroscience*, 6, 2012.
- [65] S. Hanslmayr, B. P. Staresina, and H. Bowman. Oscillations and episodic memory: Addressing the synchronization/desynchronization conundrum. *Trends in Neurosciences*, 39(1):16–25, 2016.
- [66] T. Gregor, K. Fujimoto, N. Masaki, and S. Sawai. The onset of collective behavior in social amoebae. *Science*, 328(5981):1021–1025, 2010.
- [67] T. Danino, O. Mondragón-Palomino, L. Tsimring, and J. Hasty. A synchronized quorum of genetic clocks. *Nature*, 463(7279):326–330, 2010.
- [68] R. C. Calizo, M. K. Bell, A. Ron, M. Hu, S. Bhattacharya, N. J. Wong, W. G. M. Janssen, G. Perumal, P. Pederson, S. Scarlata, J. Hone, E. U. Azeloglu, P. Rangamani, and R. Iyengar. Cell shape regulates subcellular organelle location to control early  $\text{Ca}^{2+}$  signal dynamics in vascular smooth muscle cells. *Scientific Reports*, 10(1):17866, 2020.
- [69] M. K. Bell, C. T. Lee, and P. Rangamani. Spatiotemporal modelling reveals geometric dependence of AMPAR dynamics on dendritic spine morphology. *The Journal of Physiology*, 601(15):3329–3350, 2023.

- [70] A. Leung, D. Ohadi, G. Pekkurnaz, and P. Rangamani. Systems modeling predicts that mitochondria ER contact sites regulate the postsynaptic energy landscape. *npj Systems Biology and Applications*, 7(1):26, 2021.
- [71] P. Rangamani, A. Lipshtat, E. U. Azeloglu, R. C. Calizo, M. Hu, S. Ghassemi, J. Hone, S. Scarlata, S. R. Neves, and R. Iyengar. Decoding information in cell shape. *Cell*, 154(6):1356–1369, 2013.
- [72] M. A. Alfonzo-Méndez, K. A. Sochacki, M.-P. Strub, and J. W. Taraska. Dual clathrin and integrin signaling systems regulate growth factor receptor activation. *Nature Communications*, 13(1):905, 2022.
- [73] F. Baschieri, S. Dayot, N. Elkhatib, N. Ly, A. Capmany, K. Schauer, T. Betz, D. M. Vignjevic, R. Poincloux, and G. Montagnac. Frustrated endocytosis controls contractility-independent mechanotransduction at clathrin-coated structures. *Nature Communications*, 9(1):3825, 2018.
- [74] D. Nair, E. Hosy, J. D. Petersen, A. Constals, G. Giannone, D. Choquet, and J.-B. Sibarita. Super-resolution imaging reveals that ampa receptors inside synapses are dynamically organized in nanodomains regulated by PSD95. *Journal of Neuroscience*, 33(32):13204–13224, 2013.
- [75] J. Z. Zhang, T.-W. Lu, L. M. Stolerman, B. Tenner, J. R. Yang, J.-F. Zhang, M. Falcke, P. Rangamani, S. S. Taylor, S. Mehta, and J. Zhang. Phase separation of a PKA regulatory subunit controls cAMP compartmentation and oncogenic signaling. *Cell*, 182(6):1531–1544.e15, 2020.
- [76] T. Shibasaki, H. Takahashi, T. Miki, Y. Sunaga, K. Matsumura, M. Yamanaka, C. Zhang, A. Tamamoto, T. Satoh, J. ichi Miyazaki, and S. Seino. Essential role of epac2/rap1 signaling in regulation of insulin granule dynamics by camp. *Proceedings of the National Academy of Sciences*, 104(49):19333–19338, 2007.
- [77] E. Renström, L. Eliasson, and P. Rorsman. Protein kinase a-dependent and-independent stimulation of exocytosis by camp in mouse pancreatic b-cells. *The Journal of physiology*, 502(Pt 1):105, 1997.
- [78] L. Eliasson, X. Ma, E. Renström, S. Barg, P.-O. Berggren, J. Galvanovskis, J. Gromada, X. Jing, I. Lundquist, A. Salehi, S. Sewing, and P. Rorsman. SUR1 Regulates PKA-independent

- cAMP-induced Granule Priming in Mouse Pancreatic B-cells . *Journal of General Physiology*, 121(3):181–197, 2003.
- [79] W.-J. Song, M. Seshadri, U. Ashraf, T. Mdluli, P. Mondal, M. Keil, M. Azevedo, L. Kirschner, C. Stratakis, and M. Hussain. Snapin mediates incretin action and augments glucose-dependent insulin secretion. *Cell Metabolism*, 13(3):308–319, 2011.
- [80] J. Vikman, H. Svensson, Y.-C. Huang, Y. Kang, S. A. Andersson, H. Y. Gaisano, and L. Eliasson. Truncation of snap-25 reduces the stimulatory action of camp on rapid exocytosis in insulin-secreting cells. *American Journal of Physiology-Endocrinology and Metabolism*, 297(2):E452–E461, 2009. PMID: 19509185.
- [81] Q.-F. Wan, Y. Dong, H. Yang, X. Lou, J. Ding, and T. Xu. Protein Kinase Activation Increases Insulin Secretion by Sensitizing the Secretory Machinery to Ca<sup>2+</sup> . *Journal of General Physiology*, 124(6):653–662, 2004.
- [82] A. Tengholm and E. Gylfe. camp signalling in insulin and glucagon secretion. *Diabetes, Obesity and Metabolism*, 19(S1):42–53, 2017.
- [83] J. L. Sanderson and M. L. Dell’Acqua. Akap signaling complexes in regulation of excitatory synaptic plasticity. *The Neuroscientist*, 17(3):321–336, 2011. PMID: 21498812.
- [84] I. M. Nijholt, A. M. Dolga, A. Ostroveanu, P. G. Luiten, M. Schmidt, and U. L. Eisel. Neuronal akap150 coordinates pka and epac-mediated pkb/akt phosphorylation. *Cellular Signalling*, 20(10):1715–1724, 2008.
- [85] S. Mehta and J. Zhang. Liquid–liquid phase separation drives cellular function and dysfunction in cancer. *Nature Reviews Cancer*, 22(4):239–252, 2022.
- [86] A. Boija, I. A. Klein, and R. A. Young. Biomolecular condensates and cancer. *Cancer Cell*, 39(2):174–192, 2021.
- [87] S. Jiang, J. B. Fagman, C. Chen, S. Alberti, and B. Liu. Protein phase separation and its role in tumorigenesis. *eLife*, 9:e60264, 2020.
- [88] D. Cai, Z. Liu, and J. Lippincott-Schwartz. Biomolecular condensates and their links to cancer progression. *Trends in Biochemical Sciences*, 46(7):535–549, 2021.



- [89] I. Mahmud and D. Liao. DAXX in cancer: phenomena, processes, mechanisms and regulation. *Nucleic Acids Research*, 47(15):7734–7752, 2019.
- [90] J. J. Bouchard, J. H. Otero, D. C. Scott, E. Szulc, E. W. Martin, N. Sabri, D. Granata, M. R. Marzahn, K. Lindorff-Larsen, X. Salvatella, B. A. Schulman, and T. Mittag. Cancer mutations of the tumor suppressor spop disrupt the formation of active, phase-separated compartments. *Molecular Cell*, 72(1):19–36.e8, 2018.
- [91] E. Grabocka and D. Bar-Sagi. Mutant kras enhances tumor cell fitness by upregulating stress granules. *Cell*, 167(7):1803–1813.e12, 2016.
- [92] S. P. Somasekharan, A. El-Naggar, G. Leprivier, H. Cheng, S. Hajee, T. G. Grunewald, F. Zhang, T. Ng, O. Delattre, V. Evdokimova, Y. Wang, M. Gleave, and P. H. Sorensen. YB-1 regulates stress granule formation and tumor progression by translationally activating G3BP1. *Journal of Cell Biology*, 208(7):913–929, 2015.
- [93] E. Lazzerini-Denchi and A. Sfeir. Stop pulling my strings — what telomeres taught us about the dna damage response. *Nature Reviews Molecular Cell Biology*, 17(6):364–378, 2016.
- [94] R. L. Dilley and R. A. Greenberg. Alternative telomere maintenance and cancer. *Trends in Cancer*, 1(2):145–156, 2015.
- [95] S. Kondo and T. Miura. Reaction-diffusion model as a framework for understanding biological pattern formation. *Science*, 329(5999):1616–1620, 2010.
- [96] S. Sick, S. Reinker, J. Timmer, and T. Schlake. WNT and DKK determine hair follicle spacing through a reaction-diffusion mechanism. 314(5804):1447–1450.
- [97] J. Raspopovic, L. Marcon, L. Russo, and J. Sharpe. Digit patterning is controlled by a bmp-sox9-wnt turing network modulated by morphogen gradients. *Science*, 345(6196):566–570, 2014.
- [98] T. Miura. Models of lung branching morphogenesis. *The Journal of Biochemistry*, 157(3):121–127, 2015.

- [99] Z. M. Wilmott, A. Goriely, and J. W. Raff. A simple turing reaction–diffusion model explains how PLK4 breaks symmetry during centriole duplication and assembly. *PLOS Biology*, 21(11):1–23, 2023.
- [100] D. Karig, K. M. Martini, T. Lu, N. A. DeLateur, N. Goldenfeld, and R. Weiss. Stochastic turing patterns in a synthetic bacterial population. *Proceedings of the National Academy of Sciences*, 115(26):6572–6577, 2018.
- [101] S. Ranganathan and E. I. Shakhnovich. Dynamic metastable long-living droplets formed by sticker-spacer proteins. *eLife*, 9:e56159, 2020.
- [102] H. Wang, N. S. Wingreen, and R. Mukhopadhyay. Self-organized periodicity of protein clusters in growing bacteria. *Phys. Rev. Lett.*, 101:218101, 2008.
- [103] Q.-X. Liu, A. Doelman, V. Rottschäfer, M. de Jager, P. M. J. Herman, M. Rietkerk, and J. van de Koppel. Phase separation explains a new class of self-organized spatial patterns in ecological systems. *Proceedings of the National Academy of Sciences*, 110(29):11905–11910, 2013.
- [104] K. Gasiór, M. G. Forest, A. S. Gladfelter, and J. M. Newby. Modeling the mechanisms by which coexisting biomolecular RNA–protein condensates form. *Bulletin of Mathematical Biology*, 82(12):153, 2020.
- [105] A. Mahapatra, D. Saintillan, and P. Rangamani. Curvature-driven feedback on aggregation–diffusion of proteins in lipid bilayers. *Soft Matter*, 17:8373–8386, 2021.
- [106] E. Klipp and W. Liebermeister. Mathematical modeling of intracellular signaling pathways. *BMC Neuroscience*, 7(1):S10, 2006.
- [107] A. R. Means and J. R. Dedman. Calmodulin—an intracellular calcium receptor. *Nature*, 285(5760):73–77, 1980.

## Supplement

### S1 3D reaction-diffusion model

To investigate the underlying biochemical mechanism and the effect of biophysical properties of the cell as mentioned in Figure 1B, we used the 3D reaction-diffusion model in [32] to describe the dynamics of  $\text{Ca}^{2+}$ , cAMP, and other molecules that interact with  $\text{Ca}^{2+}$  and cAMP. Next, we introduced this model and listed the equations below.

#### S1.1 Chemical species or quantities

For the  $\text{Ca}^{2+}$ -cAMP circuit, we considered 22 chemical species or quantities in total (Figure 1C). On the one hand, there are 13 chemical species in the cytosol (non-highlighted species in Figure 1C), including calcium, cAMP, CaM (calmodulin), PDE (Cyclic nucleotide phosphodiesterase), PKA (protein kinase A), and complexes of these molecules. On the other hand, there are 9 chemical species or quantities on the membrane (highlighted in yellow in Figure 1C), such as membrane voltage,  $\text{K}^+$  channel, AC (Adenylyl cyclase), AKAP, and complexes of these molecules. These molecules in the cytosol and on the membrane have been proven to play crucial roles in regulating the  $\text{Ca}^{2+}$ -cAMP pathway [8, 106, 107]. For the full list of species, we refer the readers to Table S1.

#### S1.2 Chemical reactions

The dynamics of these 22 chemical species or quantities are governed by 25 chemical reactions (v1-25 in Figure 1C). The  $\text{Ca}^{2+}$  in the cytosol can bind to CaM, leading to the activation of inactive PDE and inactive AC (v1-8). Since the inactive AC has been validated to be co-localized with AKAP by forming AKAP/AC nanodomains on the cell membrane [32], the activation of inactive AC caused by the  $\text{Ca}^{2+}$ /CaM complex is only distributed on the AKAP/AC nanodomain. Then, the active AC (denoted as AC\*) on AKAP/AC nanodomains can improve the synthesis of cAMP (v9), while the active PDE (denoted as PDE\*) degrades the cAMP in the cytosol (v10-13). Under the stimulus of cAMP, PKA in the cytosol is activated (v14-15). Another pathway to activate PKA is localized at the AKAP/AC nanodomain: AKAP binds to inactive PKA (v16-18) in the absence of cAMP, and these inactive PKA will also become active and dissociate with AKAP in the presence of cAMP (v19-20). Those active PKA can increase the synthesis of  $\text{Ca}^{2+}$  (v24-25). Besides,  $\text{Ca}^{2+}$  level is also affected by

the membrane voltage ( $v_24$ ), and the latter is modeled by the classical Hodgkin–Huxley model. The Hodgkin–Huxley model describes the dynamics of membrane voltage, and the following ion channels are taken into consideration (v21-23):  $\text{Ca}^{2+}$  channel,  $\text{K}^+$  channel,  $\text{Ca}^{2+}$  gated  $\text{K}^+$  channel, and the leak channel. For the full list of chemical reactions, we refer the readers to Table S2.

According to the type of reaction, these 25 reactions can be categorized into two classes: the first type is the production, degradation, or binding event (solid arrows in Figure 1C), and the other is the regulatory reaction (dashed arrows in Figure 1C). For the first type, the species before and after the arrow are the reactant and product, respectively. For example,  $\text{AC} + \text{Ca}_2\text{CaM} \leftrightarrow \text{CaM} \cdot \text{AC}$  means that the AC can bind to  $\text{Ca}_2\text{CaM}$  and thus form the complex  $\text{CaM} \cdot \text{AC}$ . However, for the second type, the species before the arrow regulates the chemical reaction instead of working as the reactant; for instance, the reaction v12 means that the active PDE enhances the cAMP degradation. Due to the meaning of each type, one key difference between these two types is that the species before the arrow will be consumed for the first type of reaction but not for the second type of reaction.

### S1.3 Compartment

As mentioned before, though calcium and cAMP are mostly distributed in the cytosol, they both can interact with molecules on the cell membrane, such as AKAP and AC. To take these chemical reactions on cell membrane into consideration, we chose a small compartment in one cell, that is, a hexagonal prism (Figure 1C), where the top surface (denoted by  $\Gamma$ ) represents the cell membrane and the volume under the top surface (denoted by  $\Omega$ ) the cytosol. Besides, the height and width of the compartment are set to be 600 nm and 400 nm respectively, which are consistent with those in [32]. However, in order to study the effect of the compartment size on the time delay between  $\text{Ca}^{2+}$  and cAMP, the height and width may vary, which are labeled in figures and illustrated in the main text.

### S1.4 Governing equations

To describe the dynamics of 22 chemical species in the compartment, the 3D diffusion-reaction model in [32] is adopted, which is shown as follows:

$$\left\{ \begin{array}{l} [\text{Ca}^{2+}]_t = -2j_1 - j_2 - j_3 - 2j_7 + j_{25} + D_{\text{Ca}^{2+}} \nabla^2 [\text{Ca}^{2+}] \\ [\text{CaM}]_t = -j_1 + D_{\text{CaM}} \nabla^2 [\text{CaM}] \\ [\text{Ca}_2\text{CaM}]_t = j_1 - j_2 - j_6 + D_{\text{Ca}_2\text{CaM}} \nabla^2 [\text{Ca}_2\text{CaM}] \\ [\text{Ca}_3\text{CaM}]_t = j_2 - j_3 + D_{\text{Ca}_3\text{CaM}} \nabla^2 [\text{Ca}_3\text{CaM}] \\ [\text{Ca}_4\text{CaM}]_t = j_3 - j_8 + D_{\text{Ca}_4\text{CaM}} \nabla^2 [\text{Ca}_4\text{CaM}] \\ [\text{PDE}]_t = -j_6 - j_8 + D_{\text{PDE}} \nabla^2 [\text{PDE}] \\ [\text{CaM} \cdot \text{PDE}]_t = j_6 - j_7 + D_{\text{CaM} \cdot \text{PDE}} \nabla^2 [\text{CaM} \cdot \text{PDE}] \\ [\text{PDE}^*]_t = j_7 + j_8 + D_{\text{PDE}^*} \nabla^2 [\text{PDE}^*] \\ [\text{cAMP}]_t = -j_{10} - j_{11} - j_{12} - j_{13} - 2j_{14} - 2j_{15} \\ \quad + D_{\text{cAMP}} \nabla^2 [\text{cAMP}] \\ [\text{R}_2]_t = j_{15} + D_{\text{R}_2} \nabla^2 [\text{R}_2] \\ [\text{R}_2\text{C}]_t = j_{14} - j_{15} + D_{\text{R}_2\text{C}} \nabla^2 [\text{R}_2\text{C}] \\ [\text{R}_2\text{C}_2]_t = -j_{14} + D_{\text{R}_2\text{C}_2} \nabla^2 [\text{R}_2\text{C}_2] \\ [\text{PKA}]_t = j_{14} + j_{15} + D_{\text{PKA}} \nabla^2 [\text{PKA}] \\ V_t = \frac{1}{C_m} (-I_{KCa} - I_{Ca} - I_L - I_K) + D_V \nabla_\Gamma^2 V \\ w_t = j_{23} \\ [\text{AC}]_t = -j_4 \\ [\text{CaM} \cdot \text{AC}]_t = j_4 - j_5 \\ [\text{AC}^*]_t = j_5 \\ [\text{AKAP}]_t = -j_{16} - j_{17} - j_{18} \\ [\text{AKAP-R}_2]_t = j_{18} + j_{20} \\ [\text{AKAP-R}_2\text{C}]_t = j_{19} - j_{20} + j_{17} \\ [\text{AKAP-R}_2\text{C}_2]_t = j_{16} - j_{19} \end{array} \right. \begin{array}{l} \text{in } \Omega \\ \text{on } \Gamma \end{array} \quad (\text{S1})$$

where  $[\dots]$  denotes the concentration of species except the membrane voltage  $V$  and  $\text{K}^+$  channel open probability  $w$ . The  $\Gamma$  is the top surface of the compartment, and  $\Omega$  is the volume under  $\Gamma$  (see Figure

1C). The term on the right-hand side is the time derivative, and that on the left-hand side is composed of reaction parts ( $j_1$  to  $j_{20}$ ,  $I_{KCa}/C_m$ ,  $I_{Ca}/C_m$ ,  $I_L/C_m$ ,  $I_K/C_m$ , and  $j_{23}$  to  $j_{25}$ ) and diffusion parts ( $D_X \nabla^2[X]$ ,  $X = \text{Ca}^{2+}$ ,  $\text{CaM}$ ,  $\dots$ ,  $\text{PKA}$ , and  $D_V \nabla_\Gamma^2[V]$ ). For reaction parts, the  $j_1$  to  $j_{20}$  represent the flux of reactions v1-20, respectively;  $I_{KCa}$ ,  $I_{Ca}$ ,  $I_L$ , and  $I_K$  are ion channel currents;  $C_m$  is the capacitance of cell membrane; the  $j_{23}$  to  $j_{25}$  represent the flux of reactions v23-25 respectively (see Tables S2 and S3). Note that the flux of the production, degradation or binding event (solid arrows in Figure 1C) will lead to not only the consumption of reactants but also the production of products. However, the reaction that regulates other reactions (dashed arrows in Figure 1C) only affects the reaction rate while maintaining the concentration of regulator species. As for diffusion parts, the  $D_X$  ( $X = \text{Ca}^{2+}$ ,  $\text{CaM}$ ,  $\dots$ ,  $\text{PKA}$ ,  $V$ ) denotes the diffusion coefficient of species  $X$  (see Table S4 for exact values); the  $\nabla^2$  is the Laplace operator representing  $\frac{\partial^2}{\partial x^2} + \frac{\partial^2}{\partial y^2} + \frac{\partial^2}{\partial z^2}$ ; the  $\nabla_\Gamma^2$  denotes the diffusion on the cell membrane  $\Gamma$  and is defined as  $\frac{\partial^2}{\partial x^2} + \frac{\partial^2}{\partial y^2}$ .

As for the boundary condition, most of species are assumed to have the zero flux on the boundary  $\Gamma$ , and those with non-zero fluxes on  $\Gamma$  are listed as follows:

$$\left\{ \begin{array}{l} -D_{\text{Ca}^{2+}} \vec{n} \cdot \nabla[\text{Ca}^{2+}] = j_{24} - 2j_5, \text{ on } \Gamma \\ -D_{\text{Ca}_2\text{CaM}} \vec{n} \cdot \nabla[\text{Ca}_2\text{CaM}] = -j_4, \text{ on } \Gamma \\ -D_{\text{cAMP}} \vec{n} \cdot \nabla[\text{cAMP}] = j_9 - 2j_{19} - 2j_{20}, \text{ on } \Gamma \\ -D_{\text{R}_2} \vec{n} \cdot \nabla[\text{R}_2] = -j_{18}, \text{ on } \Gamma \\ -D_{\text{R}_2\text{C}} \vec{n} \cdot \nabla[\text{R}_2\text{C}] = -j_{17}, \text{ on } \Gamma \\ -D_{\text{R}_2\text{C}_2} \vec{n} \cdot \nabla[\text{R}_2\text{C}_2] = -j_{16}, \text{ on } \Gamma \\ -D_{\text{PKA}} \vec{n} \cdot \nabla[\text{PKA}] = j_{19} + j_{20}, \text{ on } \Gamma \end{array} \right. \quad (\text{S2})$$

where  $\vec{n}$  denotes the exterior normal vector to the membrane  $\Gamma$ . These non-zero fluxes result from the reactions whose reactant or product is located on the cell membrane  $\Gamma$ . For the six surfaces surrounding the compartment, periodic boundary conditions are applied. The bottom surface is assumed to have zero fluxes.

The initial condition for species in the cytosol is set to be uniformly distributed (see Table S5 for exact values). For those species on the membrane, their initial conditions are set to be 0 except for AKAP and AC (Table S5). Since AKAP can form nanodomains [32], we used the following Gaussian distribution to model one AKAP nanodomain:

$$[\text{AKAP}]|_{t=0} = A \frac{1}{\sqrt{2\pi}\sigma} \exp\left(-\frac{1}{2} \frac{(x-x_0)^2 + (y-y_0)^2}{\sigma^2}\right), \quad (x, y) \in \Gamma \quad (\text{S3})$$

where  $\sigma$  and  $A$  are set to be 25 nm and 6.1446E11 copies/nm respectively. The  $x_0$  and  $y_0$  denote the x and y coordinates of the nanodomain center. For example, in Figure 1D where the AKAP/AC nanodomain is at the center of the cell membrane  $\Gamma$ , the  $x_0$  and  $y_0$  are both zero. Moreover, the initial concentration of AC on the cell membrane is set to be the same as that of AKAP, unless otherwise specified. Besides, the derivative of the concentration with respect to time for all species is set to be 0 at time 0 (Table S5).

### S1.5 Numerical simulations

To simulate the dynamics of all molecules in the above mathematical model, we used COMSOL Multiphysics 7.1 to numerically solve equations (S1) and (S2). The COMSOL files are available at [https://github.com/RangamaniLabUCSD/Qiao\\_et\\_al\\_cAMP-Calcium-on-AKAP-AC-nanodomains](https://github.com/RangamaniLabUCSD/Qiao_et_al_cAMP-Calcium-on-AKAP-AC-nanodomains).

## S2 A simple ODE model

To simplify the equation (1), the time  $t$  is multiplied by  $m$ , and  $v$  and  $k_1$  are normalized by  $m$ . For the simplicity of notation, we kept the notation of parameters and obtained the following equation:

$$\frac{dx}{dt} = vS(t/m) + k_1 - [S(t/m) + k_2]x.$$

It can be seen that the parameter  $m$  only influences the period of the signal. Since the period of  $\text{Ca}^{2+}$  is the same in the entire compartment, we can fix the value of  $m$  to 1 and get the equation (2).

## S3 Interaction between two nanodomains does not affect the time delay for the perfectly out-of-phase $\text{Ca}^{2+}$ -cAMP oscillation

We investigated how the distribution of AKAP/AC nanodomains affects the phase difference between  $\text{Ca}^{2+}$ -cAMP. We extended our model to include two AKAP/AC nanodomains on the cell membrane but with three distinct distances 240 nm (Figure S2A), 320 nm (Figure S2B), and 400 nm (Figure S2C). We found that the in-phase cAMP oscillation on the AKAP/AC nanodomains and perfectly out-of-phase cAMP oscillation outside the AKAP/AC nanodomains still hold (Figure S2A-D). Furthermore, the time delay for the perfectly out-of-phase case is always near 75 seconds although the distance

between two AKAP/AC nanodomains is distinct (Figure S2E). This result suggests that the distance between two AKAP/AC nanodomains has no effect on the time delay.

#### **S4 Turing pattern based AKAP/AC nanodomain**

In order to use the Turing pattern as the initial condition of AKAP/AC nanodomain, we assumed that the formation of AKAP/AC nanodomains is much faster than reactions in the  $\text{Ca}^{2+}$ -cAMP circuit, and thus we directly used the Turing pattern in the lower middle panel in Figure 7A. Note that we did not couple equation (3) into equation (S1). We also assumed that the diffusion coefficients of AKAP and AC are zero once the Turing pattern is formed, corresponding to the zero diffusion terms in the equations for AKAP and AC in the 3D reaction-diffusion model.



Table S1: Chemical species or quantities

| Abbreviation                   | Explanation  |
|--------------------------------|--|
| <b>Species in the cytosol</b>  |  |
| $\text{Ca}^{2+}$               | Calcium  |
| CaM                            | Calmodulin   |
| $\text{Ca}_2\text{CaM}$        | $\text{Ca}^{2+}$ -bound CaM with two $\text{Ca}^{2+}$ atoms              |
| $\text{Ca}_3\text{CaM}$        | $\text{Ca}^{2+}$ -bound CaM with three $\text{Ca}^{2+}$ atoms            |
| $\text{Ca}_4\text{CaM}$        | $\text{Ca}^{2+}$ -bound CaM with four $\text{Ca}^{2+}$ atoms             |
| PDE                            | Cyclic nucleotide phosphodiesterase (inactive form)                      |
| CaM · PDE                      | Complex of CaM and PDE   |
| PDE*                           | Activated PDE  |
| cAMP                           | Cyclic adenosine monophosphate   |
| $\text{R}_2$                   | Protein kinase A with only two regulatory subunits                       |
| $\text{R}_2\text{C}$           | Protein kinase A with one catalytic subunit and two regulatory subunits  |
| $\text{R}_2\text{C}_2$         | Protein kinase A with two catalytic subunits and two regulatory subunits |
| PKA                            | Active protein kinase A  |
| <b>Species on the membrane</b> |  |
| $V$                            | Membrane voltage   |
| $w$                            | $\text{K}^+$ channel open probability                                    |
| AC                             | Adenylyl cyclase (inactive form)   |
| CaM · AC                       | Complex of CaM and AC  |
| AC*                            | Activated AC   |
| AKAP                           | A-kinase anchoring protein   |
| AKAP- $\text{R}_2\text{C}_2$   | Complex of AKAP and $\text{R}_2\text{C}_2$                               |
| AKAP- $\text{R}_2\text{C}$     | Complex of AKAP and $\text{R}_2\text{C}$                                 |
| AKAP- $\text{R}_2$             | Complex of AKAP and $\text{R}_2$   |

Table S2: Chemical reactions

| #   | Reaction   | Reaction flux   |
|-----|--|---|
| v1  | $\text{Ca}^{2+} + \text{CaM} \leftrightarrow \text{Ca}_2\text{CaM}$                              | $j_1 = k_f[\text{Ca}^{2+}][\text{CaM}] - k_r[\text{Ca}_2\text{CaM}]$  |
| v2  | $\text{Ca}^{2+} + \text{Ca}_2\text{CaM} \leftrightarrow \text{Ca}_3\text{CaM}$                   | $j_2 = k_f[\text{Ca}^{2+}][\text{Ca}_2\text{CaM}] - k_r[\text{Ca}_3\text{CaM}]$                                 |
| v3  | $\text{Ca}^{2+} + \text{Ca}_3\text{CaM} \leftrightarrow \text{Ca}_4\text{CaM}$                   | $j_3 = k_f[\text{Ca}^{2+}][\text{Ca}_3\text{CaM}] - k_r[\text{Ca}_4\text{CaM}]$                                 |
| v4  | $\text{AC} + \text{Ca}_2\text{CaM} \leftrightarrow \text{CaM} \cdot \text{AC}$                   | $j_4 = k_f[\text{AC}][\text{Ca}_2\text{CaM}] - k_r[\text{CaM} \cdot \text{AC}]$                                 |
| v5  | $\text{CaM} \cdot \text{AC} + 2 \text{Ca}^{2+} \leftrightarrow \text{AC}^*$                      | $j_5 = K_{cat} \frac{[\text{Ca}^{2+}][\text{CaM} \cdot \text{AC}]}{[\text{Ca}^{2+}] + K_m} - k_r[\text{AC}^*]$  |
| v6  | $\text{PDE} + \text{Ca}_2\text{CaM} \leftrightarrow \text{CaM} \cdot \text{PDE}$                 | $j_6 = k_f[\text{PDE}][\text{Ca}_2\text{CaM}] - k_r[\text{CaM} \cdot \text{PDE}]$                               |
| v7  | $\text{CaM} \cdot \text{PDE} + 2 \text{Ca}^{2+} \leftrightarrow \text{PDE}^*$                    | $j_7 = K_{cat} \frac{[\text{Ca}^{2+}][\text{CaM} \cdot \text{PDE}]}{[\text{Ca}^{2+}] + K_m} - k_r[\text{AC}^*]$ |
| v8  | $\text{PDE} + \text{Ca}_4\text{CaM} \leftrightarrow \text{PDE}^*$                                | $j_8 = k_f[\text{PDE}][\text{Ca}_4\text{CaM}] - k_r[\text{PDE}^*]$  |
| v9  | $\rightarrow \text{cAMP}$  | $j_9 = k_{base}([\text{CaM} \cdot \text{AC}] + \text{AC}_{ind} + [\text{AC}^*]) + k_{act}[\text{AC}^*]$         |
| v10 | $\text{cAMP} \rightarrow$  | $j_{10} = k_{base}[\text{PDE}] \frac{[\text{cAMP}]}{[\text{cAMP}] + K_m}$                                       |
| v11 | $\text{cAMP} \rightarrow$  | $j_{11} = k_{base}[\text{CaM} \cdot \text{PDE}] \frac{[\text{cAMP}]}{[\text{cAMP}] + K_m}$                      |
| v12 | $\text{cAMP} \rightarrow$  | $j_{12} = k_{act}[\text{PDE}^*] \frac{[\text{cAMP}]}{[\text{cAMP}] + K_m}$                                      |
| v13 | $\text{cAMP} \rightarrow$  | $j_{13} = k_{base} \frac{[\text{cAMP}]}{[\text{cAMP}] + K_m}$   |
| v14 | $2 \text{cAMP} + \text{R}_2\text{C}_2 \leftrightarrow \text{R}_2\text{C} + \text{PKA}$           | $j_{14} = k_f[\text{cAMP}]^2[\text{R}_2\text{C}_2] - k_r[\text{R}_2\text{C}][\text{PKA}]$                       |
| v15 | $2 \text{cAMP} + \text{R}_2\text{C} \leftrightarrow \text{R}_2 + \text{PKA}$                     | $j_{15} = k_f[\text{cAMP}]^2[\text{R}_2\text{C}] - k_r[\text{R}_2][\text{PKA}]$                                 |
| v16 | $\text{AKAP} + \text{R}_2\text{C}_2 \leftrightarrow \text{AKAP-R}_2\text{C}_2$                   | $j_{16} = k_f[\text{AKAP}][\text{R}_2\text{C}_2] - k_r[\text{AKAP-R}_2\text{C}_2]$                              |
| v17 | $\text{AKAP} + \text{R}_2\text{C} \leftrightarrow \text{AKAP-R}_2\text{C}$                       | $j_{17} = k_f[\text{AKAP}][\text{R}_2\text{C}] - k_r[\text{AKAP-R}_2\text{C}]$                                  |
| v18 | $\text{AKAP} + \text{R}_2 \leftrightarrow \text{AKAP-R}_2$                                       | $j_{18} = k_f[\text{AKAP}][\text{R}_2] - k_r[\text{AKAP-R}_2]$  |
| v19 | $2 \text{cAMP} + \text{AKAP-R}_2\text{C}_2 \leftrightarrow \text{AKAP-R}_2\text{C} + \text{PKA}$ | $j_{19} = k_f[\text{cAMP}]^2[\text{AKAP-R}_2\text{C}_2] - k_r[\text{AKAP-R}_2\text{C}][\text{PKA}]$             |
| v20 | $2 \text{cAMP} + \text{AKAP-R}_2\text{C} \leftrightarrow \text{AKAP-R}_2 + \text{PKA}$           | $j_{20} = k_f[\text{cAMP}]^2[\text{AKAP-R}_2\text{C}] - k_r[\text{AKAP-R}_2][\text{PKA}]$                       |
| v21 | Ca <sup>2+</sup> gated K <sup>+</sup> channel current  | $I_{KCa} = g_{KCa}(V - E_{KCa}) \frac{[\text{Ca}^{2+}]}{[\text{Ca}^{2+}] + K_{KCa}}$                            |
|     | Ca <sup>2+</sup> channel current   | $I_{Ca} = g_{Ca}(V - E_{Ca}) \frac{1 + \tanh\left(\frac{V - v_1}{v_2}\right)}{2}$                               |
|     | Leak channel current   | $I_L = g_L(V - E_L)$  |
| v22 | K <sup>+</sup> channel current   | $I_K = g_K(V - E_K)w$   |

|     |                             |  |
|-----|-----------------------------|--|
| v23 | K <sup>+</sup> channel open | $j_{23} = \phi \left( \frac{1 + \tanh\left(\frac{V-v_3}{v_4}\right)}{2} - w \right) \cosh\left(\frac{V-v_3}{2v_4}\right)$                        |
| v24 | →Ca <sup>2+</sup>           | $j_{24} = \left( -\alpha I_{Ca} - v_{LPM}[Ca^{2+}] \right) (1 + k_{PKAV}[PKA])$  |
| v25 | →Ca <sup>2+</sup>           | $j_{25} = Ck_{IP3R}[PKA] \frac{A[Ca^{2+}](Ca_{stores} - [Ca^{2+}])}{1 + A[Ca^{2+}] + B[Ca^{2+}]^2} - \frac{V_s[Ca^{2+}]^2}{K_s^2 + [Ca^{2+}]^2}$ |

Table S3: Kinetic parameters for chemical reactions (from [32])

| Kinetic parameters     | Definitions                          | Values                                       |
|------------------------|--------------------------------------|--|
| $C_m$                  | Capacitance of cell membrane         | 5.3 pF                                       |
| $k_f$ in $j_1$         | Forward rate                         | $3.6 \text{ s}^{-1} \cdot \mu\text{M}^{-1}$  |
| $k_r$ in $j_1$         | Backward rate                        | $8 \text{ s}^{-1}$                           |
| $k_f$ in $j_2$         | Forward rate                         | $11 \text{ s}^{-1} \cdot \mu\text{M}^{-1}$   |
| $k_r$ in $j_2$         | Backward rate                        | $195 \text{ s}^{-1}$                         |
| $k_f$ in $j_3$         | Forward rate                         | $59 \text{ s}^{-1} \cdot \mu\text{M}^{-1}$   |
| $k_r$ in $j_3$         | Backward rate                        | $500 \text{ s}^{-1}$                         |
| $k_f$ in $j_4$         | Forward rate                         | $6.8 \text{ s}^{-1} \cdot \mu\text{M}^{-1}$  |
| $k_r$ in $j_4$         | Backward rate                        | $10 \text{ s}^{-1}$                          |
| $K_{cat}$ in $j_5$     | Forward rate                         | $90 \text{ s}^{-1}$                          |
| $K_m$ in $j_5$         | Activation constant                  | $1 \mu\text{M}$                              |
| $k_r$ in $j_5$         | Backward rate                        | $10 \text{ s}^{-1}$                          |
| $k_f$ in $j_6$         | Forward rate                         | $0.25 \text{ s}^{-1} \cdot \mu\text{M}^{-1}$ |
| $k_r$ in $j_6$         | Backward rate                        | $1 \text{ s}^{-1}$                           |
| $K_{cat}$ in $j_7$     | Forward rate                         | $60 \text{ s}^{-1}$                          |
| $K_m$ in $j_7$         | Half-maximal effective concentration | $1 \mu\text{M}$                              |
| $k_r$ in $j_7$         | Backward rate                        | $1 \text{ s}^{-1}$                           |
| $k_f$ in $j_8$         | Forward rate                         | $0.25 \text{ s}^{-1} \cdot \mu\text{M}^{-1}$ |
| $k_r$ in $j_8$         | Backward rate                        | $0.1 \text{ s}^{-1}$                         |
| $k_{base}$ in $j_9$    | Basal activation rate                | $0.2 \text{ s}^{-1}$                         |
| $k_{act}$ in $j_9$     | Activation rate caused by active AC  | $23.55 \text{ s}^{-1}$                       |
| $AC_{ind}$ in $j_9$    | Basal AC level                       | $3\text{E-}8 \text{ mol/m}^2$                |
| $k_{base}$ in $j_{10}$ | Basal activation rate                | $0.6 \text{ s}^{-1}$                         |
| $K_m$ in $j_{10}$      | Half-maximal effective concentration | $0.6 \mu\text{M}$                            |
| $k_{base}$ in $j_{11}$ | Basal activation rate                | $0.6 \text{ s}^{-1}$                         |
| $K_m$ in $j_{11}$      | Half-maximal effective concentration | $0.6 \mu\text{M}$                            |
| $k_{act}$ in $j_{12}$  | Activation rate for active AC        | $720 \text{ s}^{-1}$                         |

|                        |  |  |
|------------------------|--|--|
| $K_m$ in $j_{12}$      | Half-maximal effective concentration                       | 0.6 $\mu\text{M}$                            |
| $k_{base}$ in $j_{13}$ | Basal activation rate                                      | 0.25 $\mu\text{M} \cdot \text{s}^{-1}$       |
| $K_m$ in $j_{13}$      | Half-maximal effective concentration                       | 1.4 $\mu\text{M}$                            |
| $k_f$ in $j_{14}$      | Forward rate   | 33.33 $\text{s}^{-1} \cdot \mu\text{M}^{-2}$ |
| $k_r$ in $j_{14}$      | Backward rate  | 20 $\text{s}^{-1} \cdot \mu\text{M}^{-1}$    |
| $k_f$ in $j_{15}$      | Forward rate   | 33.33 $\text{s}^{-1} \cdot \mu\text{M}^{-2}$ |
| $k_r$ in $j_{15}$      | Backward rate  | 20 $\text{s}^{-1} \cdot \mu\text{M}^{-1}$    |
| $k_f$ in $j_{16}$      | Forward rate   | 1 $\text{s}^{-1} \cdot \mu\text{M}^{-1}$     |
| $k_r$ in $j_{16}$      | Backward rate  | 0.1 $\text{s}^{-1}$                          |
| $k_f$ in $j_{17}$      | Forward rate   | 1 $\text{s}^{-1} \cdot \mu\text{M}^{-1}$     |
| $k_r$ in $j_{17}$      | Backward rate  | 0.1 $\text{s}^{-1}$                          |
| $k_f$ in $j_{18}$      | Forward rate   | 1 $\text{s}^{-1} \cdot \mu\text{M}^{-1}$     |
| $k_r$ in $j_{18}$      | Backward rate  | 0.1 $\text{s}^{-1}$                          |
| $k_f$ in $j_{19}$      | Forward rate   | 33.33 $\text{s}^{-1} \cdot \mu\text{M}^{-2}$ |
| $k_r$ in $j_{19}$      | Backward rate  | 20 $\text{s}^{-1} \cdot \mu\text{M}^{-1}$    |
| $k_f$ in $j_{20}$      | Forward rate   | 33.33 $\text{s}^{-1} \cdot \mu\text{M}^{-2}$ |
| $k_r$ in $j_{20}$      | Backward rate  | 20 $\text{s}^{-1} \cdot \mu\text{M}^{-2}$    |
| $g_{KCa}$ in $I_{KCa}$ | Conductance of $\text{Ca}^{2+}$ gated $\text{K}^+$ channel | 2000 pS                                      |
| $E_{KCa}$ in $I_{KCa}$ | Voltage of $\text{Ca}^{2+}$ gated $\text{K}^+$ channel     | -75 mV                                       |
| $K_{KCa}$ in $I_{KCa}$ | Half-maximal effective concentration                       | 5 $\mu\text{M}$                              |
| $g_{Ca}$ in $I_{Ca}$   | Conductance of $\text{Ca}^{2+}$ channel                    | 600 pS                                       |
| $E_{Ca}$ in $I_{Ca}$   | Voltage of $\text{Ca}^{2+}$ channel                        | 100 mV                                       |
| $v_1$ in $I_{Ca}$      | Normalization factor                                       | -20 mV                                       |
| $v_2$ in $I_{Ca}$      | Normalization factor                                       | 24 mV  |
| $g_L$ in $I_L$         | Conductance of leak channel                                | 150 pS                                       |
| $E_L$ in $I_L$         | Voltage of leak channel                                    | -75 mV                                       |
| $g_K$ in $I_K$         | Conductance of $\text{K}^+$ channel                        | 260 pS                                       |
| $E_K$ in $I_K$         | Voltage of $\text{K}^+$ channel                            | -75 mV                                       |
| $\phi$ in $j_{23}$     | Time scale   | 35 $\text{s}^{-1}$                           |
| $v_3$ in $j_{23}$      | Normalization factor                                       | -16 mV                                       |

|   |  |  |
|---|--|--|
| $v_4$ in $j_{23}$                       | Normalization factor                   | 11.2 mV  |
| $I_{Ca}$ in $j_{24}$                    | Ca <sup>2+</sup> channel current       | See v21  |
| $\alpha$ in $j_{24}$                    | Activation rate                        | 414.6 $\mu\text{M} \cdot \text{m} \cdot \text{s}^{-1} \text{A}^{-1}$ |
| $v_{LPM}$ in $j_{24}$                   | Activation rate                        | 7.5E-9 (s · $\mu\text{M}$ ) <sup>-1</sup>                            |
| $k_{PKAV}$ in $j_{24}$                  | Activation rate                        | 100 $\mu\text{M}^{-1}$   |
| $K_s$ in $j_{25}$                       | Half-maximal effective concentration   | 10 $\mu\text{M}$   |
| $\text{Ca}_{\text{stores}}$ in $j_{25}$ | Total Ca <sup>2+</sup> in the cytosol  | 1.56 $\mu\text{M}$   |
| $V_s$ in $j_{25}$                       | Activation rate                        | 0.1 $\mu\text{M} \cdot \text{s}^{-1}$                                |
| $k_{IP3R}$ in $j_{25}$                  | Activation rate caused by IP3 receptor | 0.05 $\mu\text{M} \cdot \text{s}^{-1}$                               |
| $A$ in $j_{25}$                         | Reaction rate constant                 | 0.2869 $\mu\text{M}^{-1}$  |
| $B$ in $j_{25}$                         | Reaction rate constant                 | 2.869 $\mu\text{M}^{-2}$   |
| $C$ in $j_{25}$                         | Reaction rate constant                 | 0.2133   |

Table S4: Diffusion coefficients (from [32])

| Kinetic parameters  | Definitions                                   | Values                |
|---------------------|---|-----------------------|
| $D_{Ca^{2+}}$       | Diffusion coefficient of $Ca^{2+}$            | $100 \mu m^2 s^{-1}$  |
| $D_{CaM}$           | Diffusion coefficient of CaM                  | $10 \mu m^2 s^{-1}$   |
| $D_{Ca_2CaM}$       | Diffusion coefficient of $CaM_2CaM$           | $10 \mu m^2 s^{-1}$   |
| $D_{Ca_3CaM}$       | Diffusion coefficient of $CaM_3CaM$           | $10 \mu m^2 s^{-1}$   |
| $D_{Ca_4CaM}$       | Diffusion coefficient of $CaM_4CaM$           | $10 \mu m^2 s^{-1}$   |
| $D_{PDE}$           | Diffusion coefficient of PDE                  | $10 \mu m^2 s^{-1}$   |
| $D_{CaM \cdot PDE}$ | Diffusion coefficient of $CaM \cdot PDE$      | $10 \mu m^2 s^{-1}$   |
| $D_{PDE^*}$         | Diffusion coefficient of $PDE^*$              | $10 \mu m^2 s^{-1}$   |
| $D_{cAMP}$          | Diffusion coefficient of cAMP                 | $60 \mu m^2 s^{-1}$   |
| $D_{R_2}$           | Diffusion coefficient of $R_2$                | $10 \mu m^2 s^{-1}$   |
| $D_{R_2C}$          | Diffusion coefficient of $R_2C$               | $10 \mu m^2 s^{-1}$   |
| $D_{R_2C_2}$        | Diffusion coefficient of $R_2C_2$             | $10 \mu m^2 s^{-1}$   |
| $D_{PKA}$           | Diffusion coefficient of PKA                  | $0.01 \mu m^2 s^{-1}$ |
| $D_V$               | Diffusion coefficient of the membrane voltage | $1 \mu m^2 s^{-1}$    |

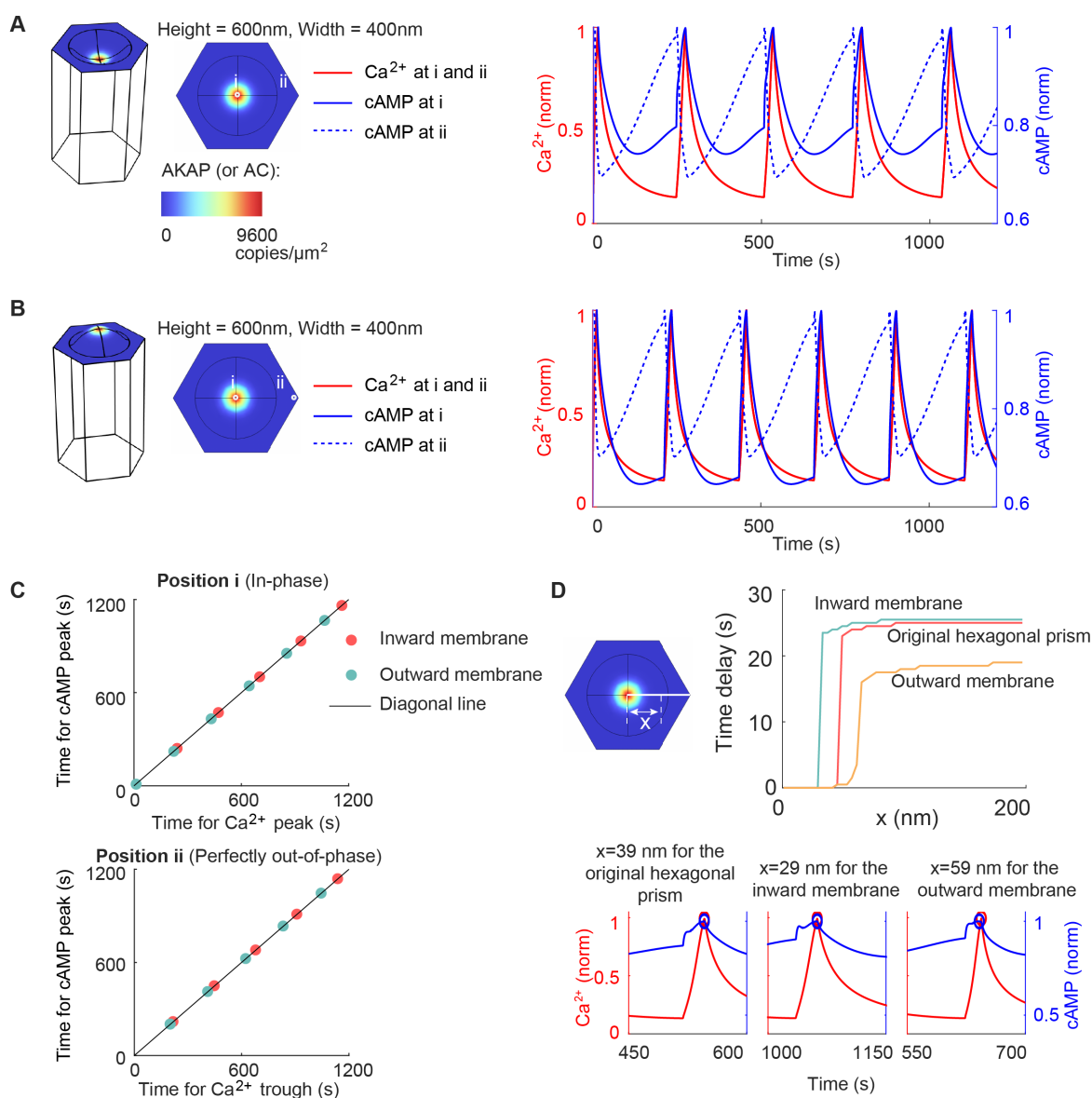
Table S5: Parameters related to initial conditions (from [32])

| Kinetic parameters                     | Definitions  | Values                     |
|--|--|----------------------------|
| $[Ca^{2+}]_0$                          | Initial condition of $[Ca^{2+}]$   | 0.001 $\mu\text{M}$        |
| $[CaM]_0$                              | Initial condition of $[CaM]$   | 2.9 $\mu\text{M}$          |
| $[Ca_2CaM]_0$                          | Initial condition of $[CaM_2CaM]$  | 0.1 $\mu\text{M}$          |
| $[Ca_3CaM]_0$                          | Initial condition of $[CaM_3CaM]$  | 4E-3 $\mu\text{M}$         |
| $[Ca_4CaM]_0$                          | Initial condition of $[CaM_4CaM]$  | 1E-2 $\mu\text{M}$         |
| $[PDE]_0$                              | Initial condition of $[PDE]$   | 0.9 $\mu\text{M}$          |
| $[CaM \cdot PDE]_0$                    | Initial condition of $[CaM \cdot PDE]$   | 1E-3 $\mu\text{M}$         |
| $[PDE^*]_0$                            | Initial condition of $[PDE^*]$   | 1E-3 $\mu\text{M}$         |
| $[cAMP]_0$                             | Initial condition of $[cAMP]$  | 4E-6 $\mu\text{M}$         |
| $[R_2]_0$                              | Initial condition of $[R_2]$   | 0.04 $\mu\text{M}$         |
| $[R_2C]_0$                             | Initial condition of $[R_2C]$  | 0                          |
| $[R_2C_2]_0$                           | Initial condition of $[R_2C_2]$  | 0.2 $\mu\text{M}$          |
| $[PKA]_0$                              | Initial condition of $[PKA]$   | 0.05 $\mu\text{M}$         |
| $V_0$                                  | Initial condition of the membrane voltage V  | -60 mV                     |
| $w_0$                                  | Initial condition of the $K^+$ channel open probability w                                  | 0                          |
| $[AC]_0$                               | Initial condition of $[AC]$  | Specified in the main text |
| $[CaM \cdot AC]_0$                     | Initial condition of $[CaM \cdot AC]$  | 0                          |
| $[AC^*]_0$                             | Initial condition of $[AC^*]$  | 0                          |
| $[AKAP]_0$                             | Initial condition of $[AKAP]$  | Specified in the main text |
| $[AKAP-R_2]_0$                         | Initial condition of $[AKAP-R_2]$  | 0                          |
| $[AKAP-R_2C]_0$                        | Initial condition of $[AKAP-R_2C]$   | 0                          |
| $[AKAP-R_2C_2]_0$                      | Initial condition of $[AKAP-R_2C_2]$   | 0                          |
| $\frac{\partial X}{\partial t} _{t=0}$ | The derivative of X w.r.t time at t= 0<br>( $X = [Ca^{2+}], [CaM], \dots, [AKAP-R_2C_2]$ ) | 0                          |

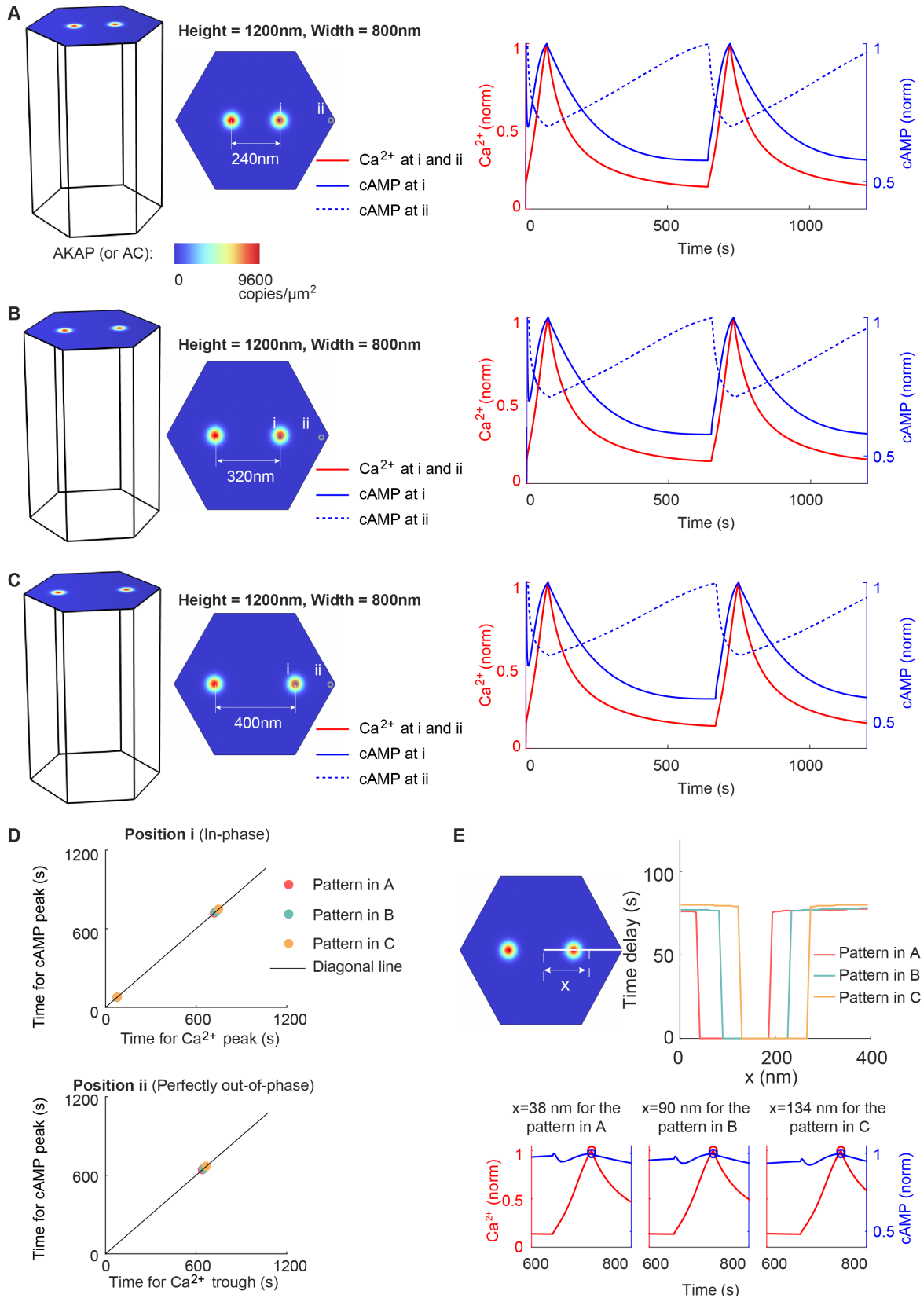


Table S6: Kinetic parameters in the Turing model (from [48])

| Kinetic parameters | Values   |
|--------------------|--|
| $b$                | $0.1 \text{ s}^{-1}$                               |
| $m_1$              | $0.04 \text{ s}^{-1}$                              |
| $m_2$              | $1 \text{ s}^{-1}$                                 |
| $\beta$            | $0.05 \text{ s}^{-1}$                              |
| $\mu$              | $0.07 \text{ s}^{-1}$                              |
| $D_r$              | $1.25 \times 10^{-3} \mu\text{m}^2 \text{ s}^{-1}$ |
| $D_s$              | $2.5 \times 10^{-5} \mu\text{m}^2 \text{ s}^{-1}$  |
| $\bar{r}$          | 0.05   |
| $\bar{s}$          | 0.05   |



**Figure S1: The effect of membrane curvature on the time delay.** (A-B) The dynamics of  $\text{Ca}^{2+}$  and cAMP for inward membrane (A) and outward membrane (B). Only two locations are considered: on the center of AKAP/AC nanodomains (i), and at the edge of the membrane (ii). (C) The in-phase and perfectly out-of-phase cAMP behavior in (A-B). (D) The time delay of peaks between  $\text{Ca}^{2+}$  and cAMP as a function of the distance  $x$  in (A-B). The  $x$  denotes the distance from the center to the edge of the cell membrane.



**Figure S2: Time delay for the perfectly out-of-phase  $\text{Ca}^{2+}$ -cAMP oscillation is not affected by the distance between two AKAP/AC nanodomains.** (A) The  $\text{Ca}^{2+}$  and cAMP dynamics where two AKAP/AC nanodomains exist on the cell membrane with a distance of 240 nm. Dynamics on one AKAP/AC nanodomain (i) and at the edge of the compartment (ii) are shown. (B-C) Same plots as (A) except for the distance between two AKAP/AC nanodomains (320 nm in B and 400 nm in C). (D) The in-phase and perfectly out-of-phase oscillations in (A-C). (E) The time delay in (A-C) as a function of the distance  $x$  to the center of the membrane compartment. The lower panel shows the magnified view of the  $\text{Ca}^{2+}$  and cAMP dynamics when  $x$  is close to the critical value, whose definition is mentioned in the caption of Figure 6E.